HOKKAIDO UNIVERSITY

Title	Stimuli-Responsive Assembly of Gold Nanorods with Uniform Orientation in Polymer Brush Substrates
Author(s)	Yang, Jingyan
Degree Grantor	北海道大学
Degree Name	博士(ソフトマター科学)
Dissertation Number	甲第16111号
Issue Date	2024-09-25
DOI	https://doi.org/10.14943/doctoral.k16111
Doc URL	https://hdl.handle.net/2115/93687
Type	doctoral thesis
File Information	Jingyan_Yang.pdf

Hokkaido University Collection of Scholarly and Academic Papers : HUSCAP

Doctoral Dissertation

Stimuli-Responsive Assembly of Gold Nanorods with Uniform Orientation in Polymer Brush Substrates

(ポリマーブラシを足場とした

均一配向化金ナノロッドの刺激応答性集合化)

Jingyan YANG

Doctor of Soft Matter Science

Graduate School of Life Sciences,

Hokkaido University

September 2024

Contents

Chapter 1 General introduction

1-1. Reversible transformation in the natural environment 6

1-2. Self-assembly in biological systems 8

1-3. Gold nanoparticles in nanotechnology 10

1-4. Assembly of gold nanoparticles 12

1-5. Assembly control of gold nanoparticles 15

1-5-1. Assembly control of gold nanoparticles on solid substrate 15

1-5-2. Assembly control of gold nanoparticles in response to external stimuli 18

1-5-3. Assembly control of gold nanoparticles with soft materials 20

1-5-4. Assembly control of gold nanoparticles with polymer brushes 22

1-6. Properties of rod-shaped gold nanoparticles 25

1-7. Uniform orientation control of gold nanorods 27

1-8. Objective 29

Chapter 2 Preparation of Cationic-Thermo-Responsive Gold Nanorods

2-1. Introduction 33

2-2. Experimental section 35

2-2-1. Materials and Instruments 35

2-2-2. Preparation of AuNRs (36 × 10 nm) 36

2-2-3. Quantification of Particle Concentration in AuNRs Dispersions 37

2-2-4. Surface modification of AuNRs with two types of thiol-ligands 38

2-2-5. Evaluation of temperature responsiveness of cTR-AuNRs with different ratio of the cationic ligand 39

2-2-6. Sigmoidal Curve Fitting for Generalization of AuNR response temperature 39

2-2-7. Time course experiments on assembly/disassembly process 39

2-2-8. Evaluation of cTR-AuNRs assembly by Finite Difference Time Domain Method 40

2-3. Results and Discussion 40

2-3-1. Evaluation of the shape of CTAB coated AuNRs 40
2-3-2. Evaluation of the modified of cTR-AuNRs with different cationic ligand ratio 42
2-3-3. Evaluation of temperature responsiveness of cTR-AuNRs with different cationic ligand ratio 43
2-3-4. Evaluation of cTR-AuNRs assembly by Finite Difference Time Domain Method 49
2-4. Conclusion 51

Chapter 3 Assembly/disassembly of Cationic-Thermo-responsive Gold Nanorods in polymer brushes with vertical alignment

3-1. Introduction 53
3-2. Experimental section 54
3-2-1. Materials and Instruments 54
3-2-2. Synthesis of double-stranded DNA 55
3-2-3. Preparation of DNA brushes 56
3-2-4. Calculation of the DNA density on polymer brushes 59
3-2-5. Calculation of the AuNRs attachment density on polymer brushes 60
3-2-6. Surface modification of AuNRs with two types of thiol-ligands 61
3-2-7. Attachment of cTR-AuNRs into DNA polymer brushes 61
3-2-8. Baseline of the p- and s-polarization 61
3-2-9. Sigmoidal Curve Fitting for Generalization of AuNR response temperature 62
3-2-10. Evaluation of cTR-AuNRs orientation and assembly into DNA polymer brushes by Finite Difference Time Domain Method 62
3-2-11. Time course experiments on assembly/disassembly process 62
3-3. Results and discussion 63
3-3-1. Synthesis of double-stranded DNA 63
3-3-2. Evaluation of double-stranded DNA polymer brushes on substrates 64
3-3-3. Evaluation of attachment of cTR-AuNRs with different cationic ligand ratio into double-stranded DNA polymer brushes 65
3-3-4. Evaluation of cTR-AuNRs reversible assembly change on double-stranded DNA polymer brushes by temperature change 71

3-3-5. Evaluation of cTR-AuNRs reversible assembly change on single-stranded DNA polymer brushes by temperature change 79
3-3-6. Evaluation of cTR-AuNRs assembly on double-stranded DNA polymer brushes by Finite Difference Time Domain Method 81
3-3-7. Evaluation of different attachment density of cTR-AuNRs assembly on double-stranded DNA polymer brushes 83
3-4. Conclusion 87

Chapter 4 General conclusion **88**

References **91**

List of academic presentation **102**

Acknowledgement **105**

Chapter 1

General introduction

1-1. Reversible transformation in the natural environment

In the natural environment, many entities exhibit sophisticated functionalities through clever manipulation of structural transformations. A prime example is the process of signal transduction across cell membranes, in which membrane proteins play a central role.[1,2] Extracellular stimuli are captured by receptor molecules that induce the formation of protein dimers within the membrane (Figure 1-1).[3,4] These dimers undergo spatial rearrangements that facilitate the transduction of extracellular signals into the intracellular environment through structural modifications of the proteins involved.

To further illustrate the importance of reversible structural changes, liquid crystal molecules provide an excellent example of artificial materials that effectively exploit such changes.[5,6] These molecules, characterized by their inherent anisotropic properties, are uniformly oriented to exhibit polarization properties. Crucially, their orientation can be dynamically changed by the application of an external voltage, enabling them to act as optical switches (Figure 1-2a).[7] By precisely controlling the alignment of liquid crystals, dynamic and reversible color changes under temperature stimuli can be achieved, allowing actuators to mimic the color-changing capabilities of natural organisms (Figure 1-2b).[8] This capability underpins the widespread use of liquid crystal displays (LCDs) and underscores the broad applicability and importance of reversible structural transformations in both natural and synthetic systems.[9,10]

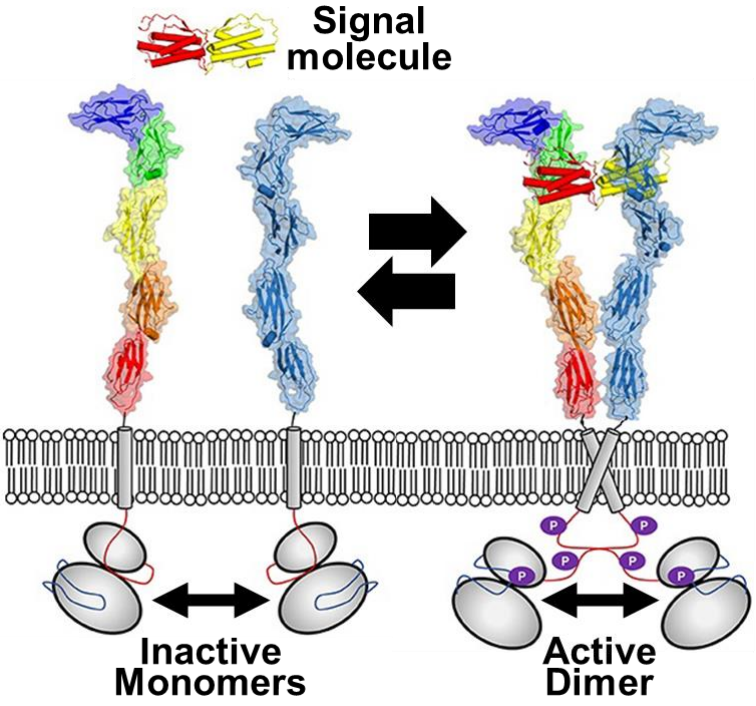


Figure 1-1. Scheme of membrane protein signal transduction.[3]

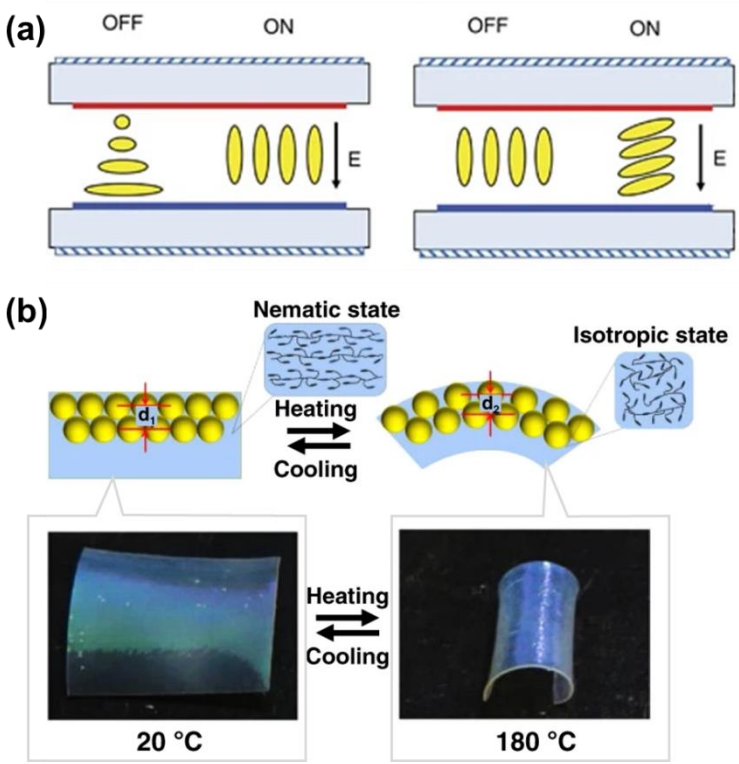


Figure 1-2. Liquid crystal molecules reversible structural change. (a) Electric field.[7] (b) Temperature.[8]

1-2. Self-assembly in biological systems

Self-assembly in biological systems is a fundamental and intricate process in which molecules spontaneously organize into well-defined structures and functional units without external guidance.[11,12] This phenomenon is central to the formation of various complex biological structures such as cell membranes, protein complexes, and DNA helices. These structures are essential for carrying out a wide range of biological functions that sustain life.

At the molecular level, self-assembly is driven by non-covalent interactions, including hydrogen bonds, van der Waals forces, hydrophobic interactions, and electrostatic interactions.[13–15] These weak but specific interactions allow the precise and reversible formation of complex assemblies from simple building blocks. For example, the lipid bilayer of cell membranes self-assembles through the hydrophobic effect, where hydrophobic tails of phospholipids aggregate away from water to form a stable membrane structure that is critical for cellular integrity and function.[16,17] Proteins, the workhorses of the cell, also rely heavily on self-assembly. Enzymes and structural proteins fold into specific three-dimensional shapes necessary for their activity, guided by their amino acid sequences and the surrounding environment.[18–20] Protein-protein interactions also enable the formation of large multiprotein complexes that are essential for processes such as signal transduction, cellular scaffolding, and molecular motor function (Figure 1-3).[21]

Understanding self-assembly in biological systems not only provides insights into fundamental life processes, but also inspires innovations in nanotechnology, medicine, and materials science. For example, researchers are exploring how to mimic self-assembly to create nanomaterials for drug delivery systems that can specifically target diseased cells, reducing side effects and improving therapeutic efficacy.[22–26] In synthetic

biology, self-assembly principles are being used to create novel biological systems and devices, from artificial enzymes to synthetic cells.[27–30]

In summary, self-assembly is a cornerstone of biological organization and function, underpinning the complexity and diversity of life. By harnessing and mimicking these natural processes, we can make significant advances in various fields of science and technology, paving the way for new medical therapies, innovative materials, and a deeper understanding of the molecular basis of life.

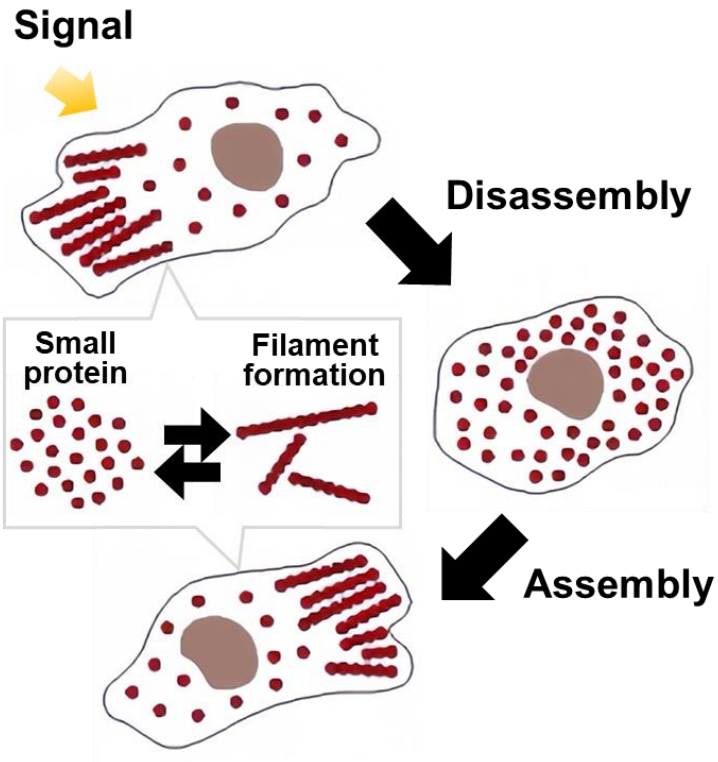


Figure 1-3. Self-assembly in biological system.[21]

1-3. Gold nanoparticles in nanotechnology

Nanoparticles are synthesized using a bottom-up approach, progressing from the atomic or molecular scale to more complex structures (Figure 1-4).[31] This method is particularly relevant to the formation of metal nanoparticles, tiny conglomerates of metal atoms characterized by a significant surface-to-volume ratio.[32–34] These nanoparticles exhibit properties significantly different from those of bulk metals and isolated atoms, providing unique functionalities in electrical, optical, and magnetic applications.[35–37] A prime example of these properties is the localized surface plasmon resonance (LSPR) phenomenon observed in nanoparticles of metals such as gold, silver, copper, and platinum (Figure 1-5).[38] In this phenomenon, free electrons localized on the nanoparticle surface undergo collective oscillations that resonate with the electromagnetic field of incident light, resulting in the selective absorption of specific wavelengths. The resonance state of these electrons is influenced by factors such as the size,[39] shape[40] and surface state of the nanoparticles, as well as their environmental context and spatial arrangement.[41–43] Consequently, the optical properties of these nanoparticles can be precisely engineered by manipulating these variables. Among various metal nanoparticles, gold nanoparticles (AuNPs) are particularly noteworthy and have been extensively studied for their ease of customization in size and shape, robust stability, and exceptional biocompatibility.[44]

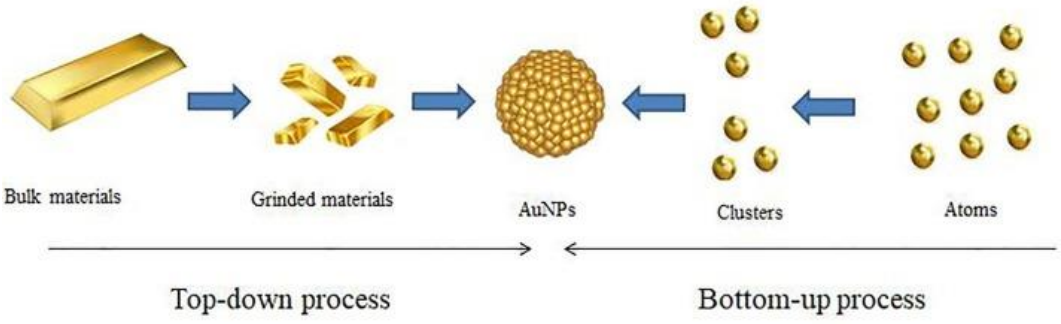


Figure 1-4. Top-down and bottom-up approaches for the synthesis of AuNPs.[31]

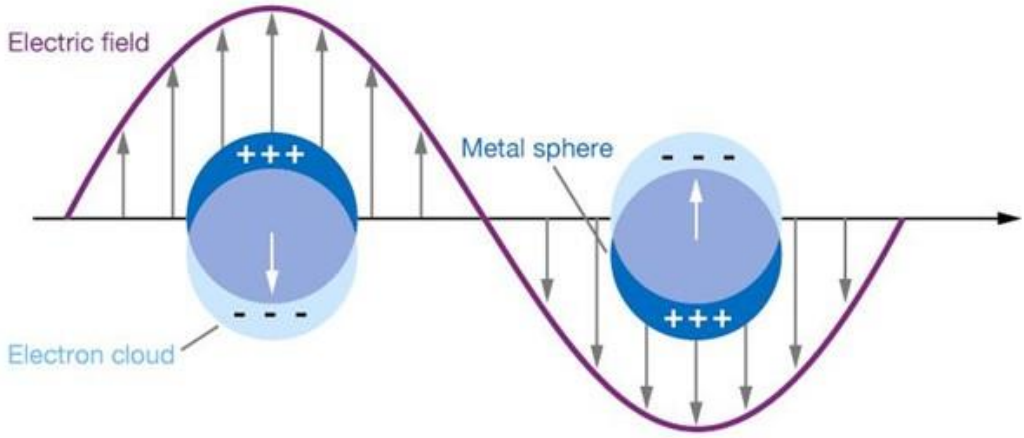


Figure 1-5. Schematic of localized surface plasmon resonance. Surface oscillations of free electron clouds relative to ion nuclei on metal surfaces.[38]

1-4. Assembly of gold nanoparticles

Gold nanoparticles (AuNPs) exhibit unique physical and chemical properties that have attracted considerable interest in various scientific fields.[45–47] One of the most intriguing properties of AuNPs is their ability to self-assemble into organized structures. This self-assembly is driven by a combination of van der Waals forces, electrostatic interactions, hydrogen bonding, and sometimes specific ligand-receptor interactions.[48] By manipulating surface chemistry, environmental conditions, and nanoparticle concentration, researchers can precisely control the self-assembly process. Surface functionalization with specific ligands or molecules influences the interactions between particles, resulting in diverse assembly patterns (Figure 1-6).[49–52] In addition, the concentration of nanoparticles in a solution determines whether they form isolated clusters or extensive networks.[53,54]

The resulting self-assembled structures can take various forms, including one-dimensional chains, two-dimensional sheets, and three-dimensional networks. One-dimensional chains are valuable for creating conductive pathways and are being investigated for their potential in nanoelectronics.[55] Two-dimensional sheets, often resembling a honeycomb pattern, have applications in sensing and surface-enhanced Raman spectroscopy (SERS).[56] Three-dimensional networks that mimic the porosity of natural materials are being explored for catalytic and filtration applications.[57]

Self-assembled AuNPs have a wide range of applications.[58–60] In catalysis, the high surface area of these structures enhances their catalytic properties, making them suitable for various chemical reactions.[61] In sensing, the unique optical properties of AuNP assemblies, such as localized surface plasmon resonance (LSPR), are exploited to develop highly sensitive biosensors.[62] For drug delivery, AuNPs can be engineered into specific

shapes and sizes to optimize drug loading and release, improving the efficacy of targeted delivery systems.[63] In materials science, self-assembled AuNPs are used to create advanced materials with tailored electronic, optical and mechanical properties, driving innovation in nanotechnology.[64,65]

In summary, self-assembly of gold nanoparticles is a versatile and powerful tool in nanotechnology, enabling the creation of complex structures with diverse applications.[66] By understanding and controlling the factors that influence self-assembly, researchers can design and fabricate nanomaterials with specific functionalities, advancing the fields of catalysis,[67] sensing,[68] drug delivery,[69,70] and materials science.[71] The ongoing study of AuNP self-assembly promises to unlock new technological innovations and improve existing applications.

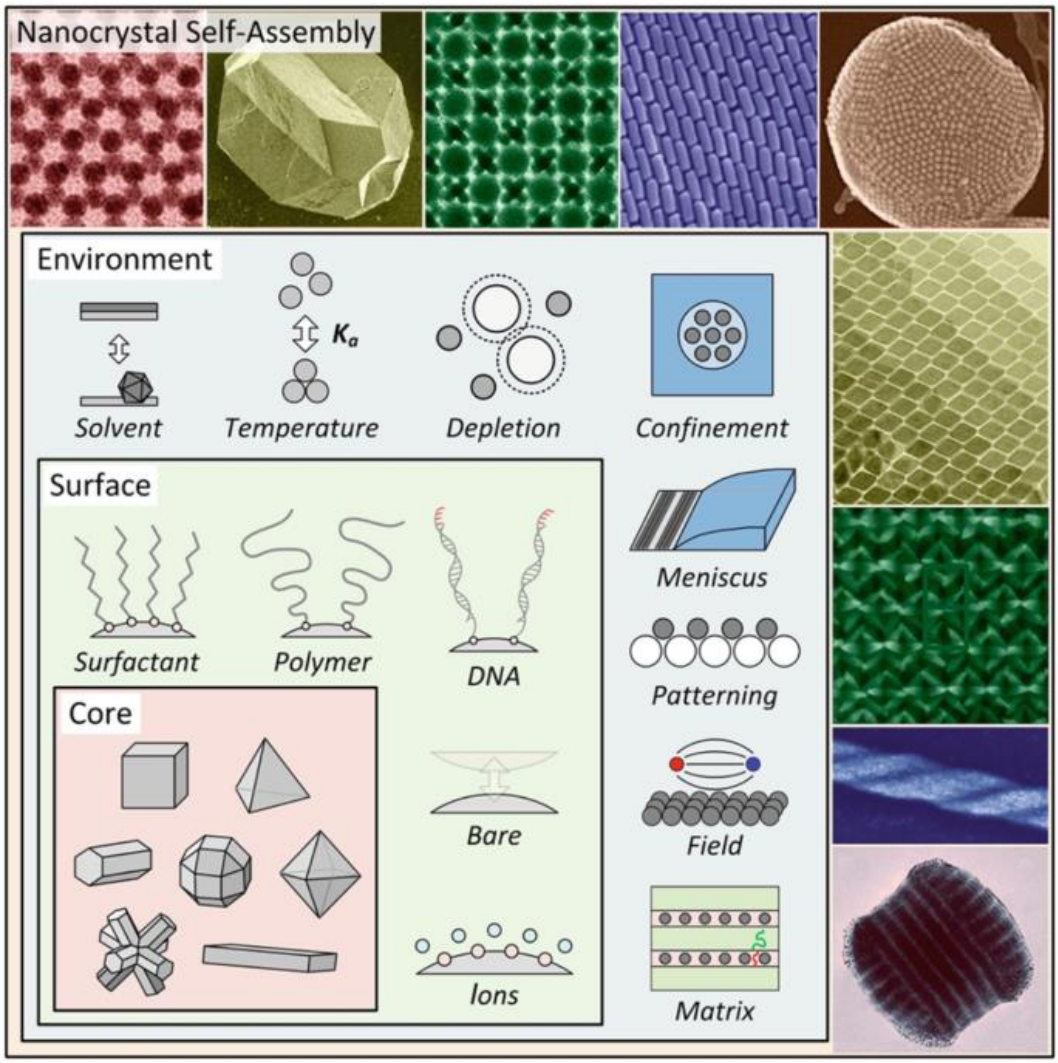


Figure 1-6. Scheme of nanoparticle self-assembly.[49]

1-5. Assembly control of gold nanoparticles

1-5-1. Assembly control of gold nanoparticles on solid substrate

Self-assembly of AuNPs on solid substrates is an important nanotechnology method that is widely used in fields such as biosensing, optical materials, and electronic devices. This self-assembly method enables the ordered arrangement of AuNPs on solid substrates through physical or chemical interactions.[72,73] For example, solution deposition can be used to uniformly deposit AuNPs on silicon substrates to form a uniform nanoparticle film (Figure 1-7a).[74] Another example is the use of self-assembled monolayer (SAM) techniques, where specific organic molecules are modified on a metal substrate to induce self-assembly of AuNPs at specific sites (Figure 1-7b).[75] Electrochemical deposition is also a commonly used method, where the precise deposition of AuNPs on a substrate is achieved by controlling the electrochemical conditions, resulting in highly ordered nanostructures.[76]

The main advantages of using solid substrates for AuNP self-assembly are their high precision and stability.[77] By manipulating the chemical modification and physical patterning of the substrate surface, the precise arrangement of nanoparticles can be achieved. This method allows researchers to design and fabricate complex nanostructures, providing significant flexibility in nanotechnology applications.[78,79] In addition, self-assembled structures on solid substrates typically exhibit high stability and are less susceptible to variations in external environmental conditions. This stability ensures the fixation of nanoparticles on the substrate, leading to excellent reproducibility and reliability in repeated experiments and practical applications. For example, in optical sensors, the ordered arrangement of AuNPs can significantly enhance the sensitivity and selectivity of the sensor.[80–82]

However, solid-state self-assembly methods also have certain drawbacks. First and foremost, the fabrication processes for solid-state self-assembly methods are relatively complex and require precise control of various conditions, which increases the complexity and cost of the experiments. In addition, the immobilization of AuNPs on a solid surface can limit their mobility. This fixation limits the adaptability and functional diversity of the resulting nanostructures, which can affect performance in certain application scenarios. For example, in biosensing applications that require dynamic adjustment, the fixed AuNP structures may not adapt well to rapidly changing detection environments.

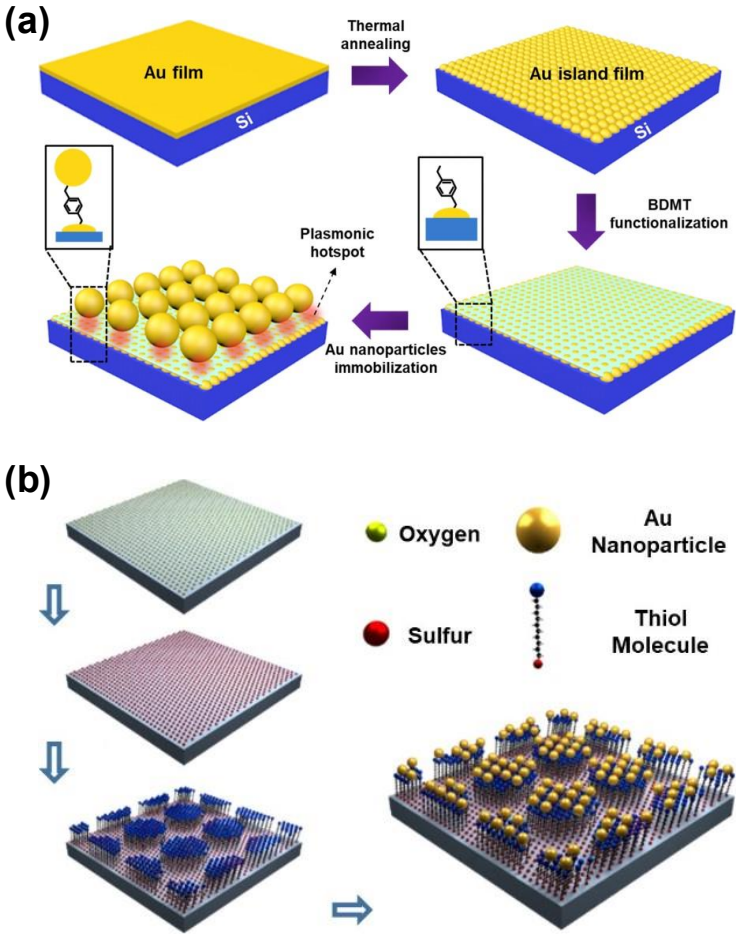


Figure 1-7. AuNPs assembly on solid substrate. (a) Solution deposition method.[74] (b) SAM techniques.[75]

1-5-2. Assembly control of gold nanoparticles in response to external stimuli

Conversely, dynamic control of nanostructures has recently become a focus of plasmonic research. Among various strategies, the assembly/disassembly of gold nanoparticles (AuNPs) in response to external stimuli such as magnetic[83,84] and electric fields,[85–89] pH,[90–94] light,[95–98] and temperature[99–104] represents a simple and effective approach. These dynamic processes not only induce significant spectral shifts, but also generate strong electromagnetic fields in the interparticle gaps, thereby enhancing the detection capabilities of surface-enhanced Raman scattering (SERS).

Dynamic control of solution-dispersed AuNPs offers significant advantages, including the ability to adjust nanostructure configurations in real-time through stimulation (Figure 1-8).[105] This flexibility is particularly beneficial in applications that require rapid and reversible changes, such as real-time sensing and adaptive optics. For example, temperature stimuli can induce the assembly or dispersion of thermo-responsive polymer-coated AuNPs.[99–102,104] As the temperature changes, these particles can dynamically adjust their arrangement, enabling reversible control of plasmonic properties.

Despite these advantages, several challenges remain. First, the tunability of the assembly size in solution-dispersed AuNPs is often limited because it is difficult to uniformly control particle assembly and separation on a large scale. In addition, maintaining the stability of dynamically controlled structures is problematic, as these structures are susceptible to destabilization by environmental factors such as temperature fluctuations and solvent conditions.[106] This instability can lead to performance inconsistencies and reduce the overall reliability of the nanostructures in practical applications.

In addition, the transition from solution-based dynamic control to device fabrication poses significant hurdles. Integrating dynamically controlled AuNPs into solid-state devices requires overcoming issues related to particle immobilization while preserving their dynamic response. This often requires sophisticated fabrication techniques and materials engineering to create hybrid systems that can maintain the desired dynamic properties without compromising structural integrity.

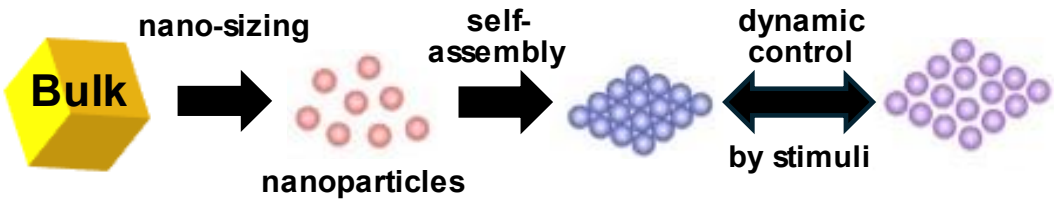


Figure 1-8. Schematic illustration of dynamic control of the nanoparticle structures by the use of external stimuli to switch or tune their properties or functions.[105]

1-5-3. Assembly control of gold nanoparticles with soft materials

In contrast, soft materials such as elastomers[107–109] and hydrogels[110–113] provide a versatile platform for the dynamic manipulation of gold nanoparticle (AuNP) configurations through mechanical actions such as stretching, compression, and volumetric changes. These materials enhance the tunability and stability of AuNP assemblies either through surface attachment or encapsulation within the materials.

Soft materials such as elastomers and hydrogels offer significant advantages for dynamic control of nanostructures. They have inherent flexibility that allows for substantial deformation without loss of structural integrity.[114] This flexibility allows real-time adjustment of AuNP configurations by mechanical stimuli. For example, hydrogels embedded with AuNPs can increase interparticle distance when stretched and decrease it when compressed, dynamically modulating plasmonic properties and enhancing surface-enhanced Raman scattering (SERS) signals.[115,116] This mechanical responsiveness is particularly advantageous for applications requiring real-time adjustment of nanostructure configurations.

Beyond configuration control, elastomers and hydrogels also significantly enhance the stability and tunability of nanostructures. Encapsulation of AuNPs in these materials effectively prevents particle aggregation or detachment, ensuring structural integrity and configuration stability during mechanical manipulation.[117–119] In addition, the tunable nature of soft materials allows them to adapt to different application needs. For example, in the field of biosensing, adjusting the mechanical properties of hydrogels can precisely control the interparticle distance of AuNPs, facilitating highly sensitive detection of various biomolecules (Figure 1-9).[120]

However, the integration of AuNPs with elastomers and hydrogels presents several challenges. The mechanical properties of these soft materials must be carefully designed to withstand repeated deformation without compromising functional integrity. In addition, the encapsulation or surface attachment of AuNPs must be sufficiently stable to prevent particle aggregation or detachment during mechanical manipulation. These requirements necessitate advanced material design and precise manufacturing techniques to produce robust and reliable dynamic SERS substrates.

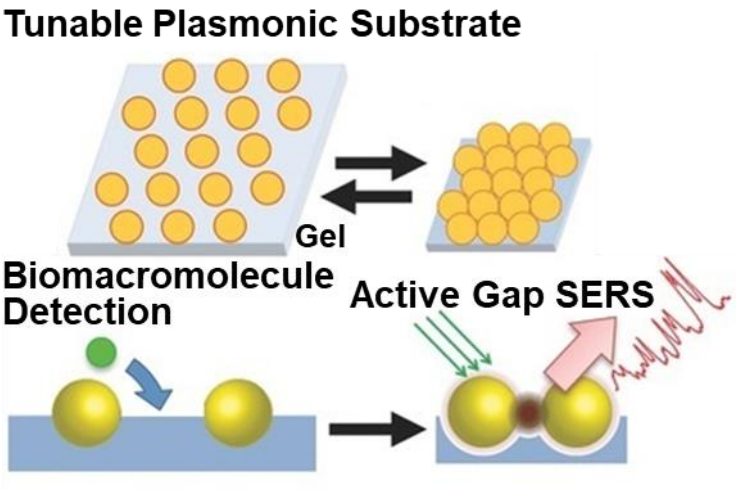


Figure 1-9. The AuNPs assembly control by soft materials.[120]

1-5-4. Assembly control of gold nanoparticles with polymer brushes

Polymer brushes, which are polymer layers attached to solid substrates, have emerged as a highly advantageous medium for the dynamic control of nanostructures due to their ability to change their structure through the movement of polymer chains. Over the past two decades, significant progress has been made in actively controlling the plasmonic properties of gold nanoparticles (AuNPs) integrated with polymer brushes by modulating the proximity of the nanoparticles.[121–125]

Polymer brushes offer several advantages for dynamic control of nanostructures. The flexible polymer chains can undergo conformational changes in response to various stimuli such as pH, temperature,[126] and solvent composition. This adaptability allows precise control of the spatial arrangement of AuNPs embedded in or attached to the polymer brushes. For example, the assembly of AuNPs within a polymer brush can be controlled by adjusting the salt concentration. Specifically, the polymer brush provides an environment that restricts the movement of the nanoparticles. When salt is added to the solution, the ions shield the negative charges on the surface of the AuNPs, reducing the electrostatic repulsion between them. This reduction in repulsion allows the AuNPs to come closer together and assemble more easily. Consequently, the degree of assembly of gold nanoparticles within the polymer brush can be modulated by controlling the salt concentration (Figure 1-10).[127] This dynamic control is particularly useful for applications that require reversible and tunable plasmonic properties.

Significant progress has been made in integrating AuNPs with polymer brushes to achieve active control of their plasmonic properties. By manipulating the proximity of the nanoparticles, researchers have developed methods to finely tune the optical and electronic properties of the nanostructures. For example, in biosensing applications, the

controlled assembly and disassembly of AuNPs within polymer brushes can enhance the sensitivity and selectivity of the sensors.[128] This level of control enables the detection of target molecules with high precision and reliability.

In addition, the versatility of polymer brushes extends to their stability and functionalization potential. The robust attachment of polymer brushes to solid substrates ensures the stability of the nanostructures under various environmental conditions. In addition, polymer brushes can be functionalized with a wide range of chemical groups, allowing the integration of AuNPs with different functionalities.[129–132] This flexibility makes polymer brushes an ideal platform for creating multifunctional nanostructures tailored for specific applications.

Overall, polymer brushes provide a versatile and robust medium for the dynamic manipulation of AuNP configurations. Their adaptability, stability, and functionalization potential make them highly suitable for advanced applications in fields such as biosensing and optoelectronics. Future research should focus on refining the synthesis and integration techniques of polymer brushes to fully exploit their capabilities in dynamic plasmonic applications.

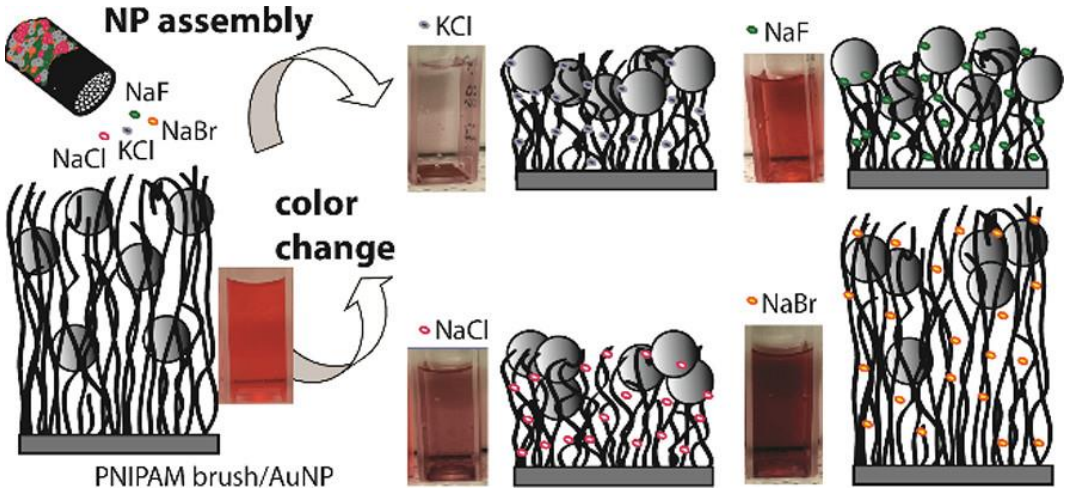


Figure 1-10. The AuNPs assembly control by polymer brush.[127]

1-6. Properties of rod-shaped gold nanoparticles

AuNPs can be synthesized in a variety of shapes. These nanoparticles are typically divided into two broad categories: isotropic and anisotropic. Isotropic nanoparticles include spherical gold nanoparticles, which are the most common due to their relative ease of synthesis and uniformity in size and shape. On the other hand, anisotropic nanoparticles, which include structures such as rod-shaped and triangular gold nanoparticles, often have more complex morphologies.[133]

Anisotropic gold nanoparticles are particularly notable for their complex structures, which present challenges in terms of controlling their assembly and functional properties. However, this complexity also confers unique optical and electronic properties not found in isotropic nanoparticles. An illustrative example is gold nanorods (AuNRs), which are characterized by their dual plasmon absorption peaks. These include the transverse localized surface plasmon resonance (T-LSPR) and the longitudinal localized surface plasmon resonance (L-LSPR) (Figure 1-11).[134]

The sensitivity of L-LSPR to the aspect ratio of AuNRs is particularly important because it allows precise tuning of their optical properties (Figure 1-12).[135] By adjusting the aspect ratio, it is possible to shift the absorption wavelength from the visible light spectrum into the near infrared. This tunability makes AuNRs extremely valuable in applications such as photothermal therapy, where their ability to absorb specific wavelengths can be used to selectively target and destroy cancer cells.[136]

Thus, while the synthesis and manipulation of anisotropic gold nanoparticles such as AuNRs are more challenging than their isotropic counterparts, their advanced properties and the potential for precise control over their optical responses open up significant opportunities for innovation in various scientific and industrial fields.

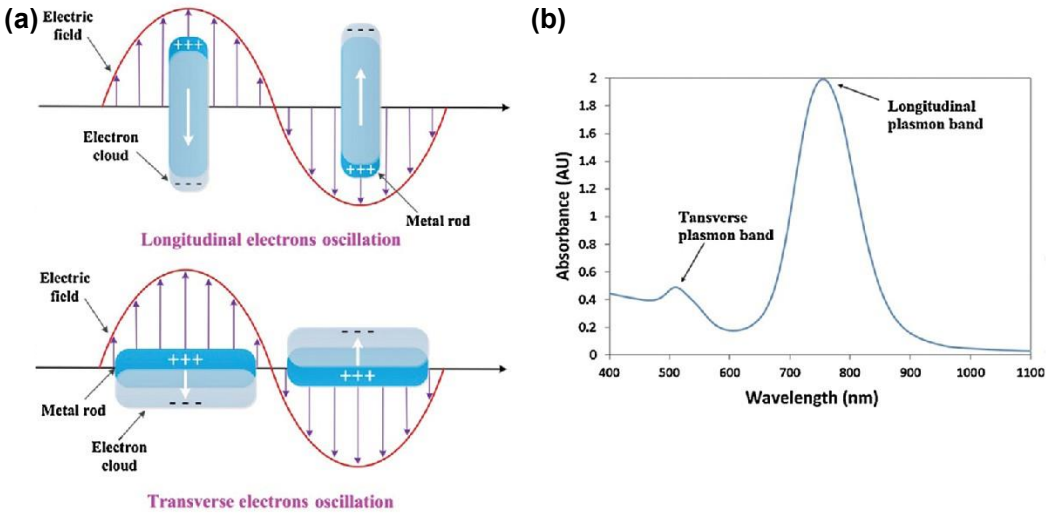


Figure 1-11. Two types of localized surface plasmon resonance (LSPR) exhibited by AuNRs. (a) Long-axis (top) or short-axis (bottom) electronic vibration. (b) Absorbance spectrum of AuNRs by LSPR.[134]

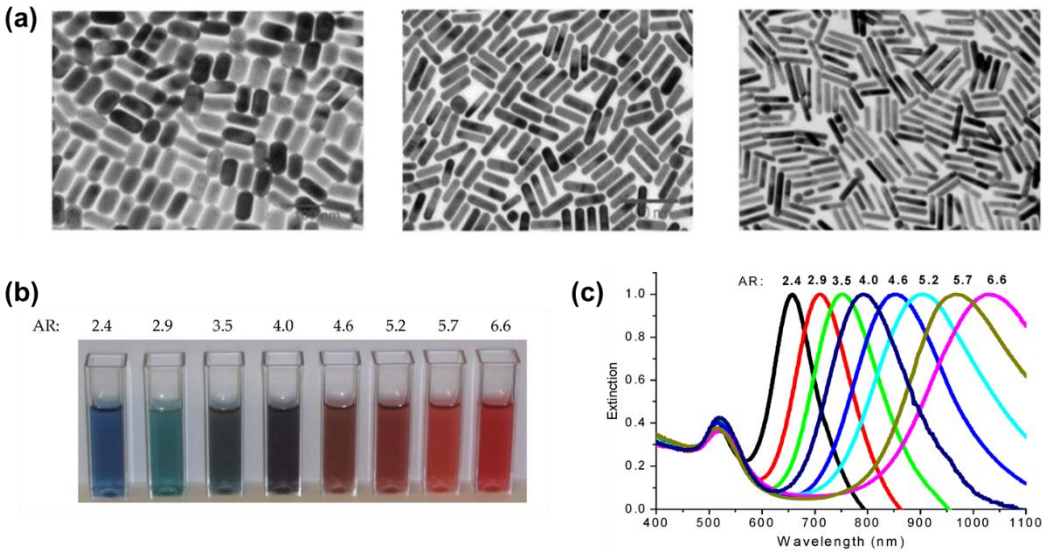


Figure 1-12. Optical characteristics of AuNRs according to aspect ratio. (a) STEM image of AuNRs. (b) Photographs of AuNR solutions of various aspect ratios. (c) Extinction spectrum of AuNRs with different aspect ratios.[135]

1-7. Uniform orientation control of gold nanorods

The anisotropic nature of AuNRs endows them with direction-dependent optical, electrical, and chemical properties. In particular, the L-LSPR of AuNRs is highly dependent on their orientation (Figure 1-13).[137] L-LSPR is a phenomenon characterized by the collective oscillation of electrons in response to light interaction, which significantly enhances the local electromagnetic field. Uniformly aligned AuNRs can maximize this effect, thereby significantly improving their performance in various applications. [138–144]

In the optical domain, the enhancement of L-LSPR is critical for techniques such as surface-enhanced Raman scattering (SERS). SERS utilizes the L-LSPR effect of AuNRs to enhance the Raman signal of molecules, enabling highly sensitive detection.[145,146] When AuNRs are uniformly aligned, their L-LSPR effect is maximized, resulting in a significant increase in SERS detection sensitivity. This is particularly important for the detection of low-concentration molecules, with critical applications in biosensing and environmental monitoring.

In electronic devices, uniformly aligned AuNRs can form nanostructures with high conductivity. Since the conductivity of gold nanorods is strongest along their longitudinal axis, uniform alignment ensures efficient electron transport between the nanorods, thereby improving the overall performance of the device. For example, in field-effect transistors (FETs), uniformly aligned AuNRs can significantly reduce electron scattering, thereby increasing conductivity and switching speed. [147,148]

In addition, the catalytic performance of AuNRs is also affected by their directional orientation. Uniformly oriented AuNRs can optimize the exposure of surface-active sites, thereby increasing the catalytic reaction efficiency. For example, in electrocatalytic water

splitting, uniformly oriented AuNRs can provide more active sites, significantly increasing the reaction rate and product selectivity.[149–151]

However, achieving uniform orientation control of AuNRs presents significant challenges. It requires precise synthesis and assembly techniques to ensure uniform alignment on a macroscopic scale. In addition, the stability of AuNRs under various environmental conditions must be studied and optimized to ensure reliability in practical applications. Researchers are exploring various methods, including self-assembly techniques, template-guided methods, and external field-assisted assembly, to achieve large-scale and stable uniform orientation control.

In summary, controlling the uniform orientation of AuNRs is crucial for maximizing their L-LSPR intensity and enhancing their performance in optical, electronic, and catalytic applications.

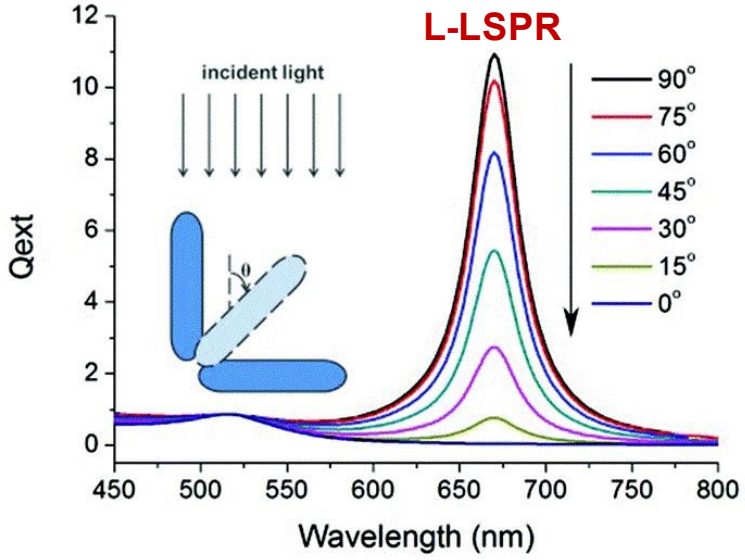


Figure 1-13. Orientation-dependent L-LSPR intensity change of AuNRs in relation to irradiated light.[137]

1-8. Objective

In our group, we have investigated the reversible assembly of gold nanorods (AuNRs) in solution.[99,100] When modified with a temperature-responsive ligand, AuNRs exhibit hydrophilic behavior and remain dispersed at low temperatures due to hydration. As the temperature increases, the AuNRs become dehydrated and transition to a hydrophobic state. This temperature-induced hydrophobic interaction leads to the assembly of AuNRs. These results demonstrate that temperature-responsive ligand-modified AuNRs can undergo reversible assembly in solution. However, the orientation of the assembled AuNRs in solution is random, limiting their potential applications.

Conversely, we have also explored the orientation control of AuNRs using DNA brushes as a substrate.[152,153] AuNRs modified with both cationic and neutral ligands were attached to the DNA brushes. At low ratios of the cationic ligand, the AuNRs are vertically aligned to the substrate. This DNA brush system demonstrates the capability to control the orientation of AuNRs. However, this system does not facilitate the reversible assembly of AuNRs.

In this research, I aim to address the limitations of both systems by working on the assembly of AuNRs within DNA brushes. Specifically, AuNRs modified with a combination of a temperature-responsive ligand and a cationic ligand will be attached to DNA brushes through electrostatic interactions. It is hypothesized that the temperature-responsive AuNRs will transition between hydrated and dehydrated states in response to temperature changes, thereby enabling reversible assembly (Figure 1-14). This approach aims to achieve reversible control of AuNR assembly while maintaining uniform orientation, potentially overcoming the limitations of random orientation in solution and irreversible assembly in DNA brush systems.

In Chapter 2, my research focuses on investigating the thermo-responsiveness of gold nanorods (AuNRs) modified with cationic and thermo-responsive ligands. I prepared cationic-thermo-responsive AuNRs (cTR-AuNRs) and adjusted their surface potential by varying the ratio of cationic ligands. The thermo-responsiveness of these cTR-AuNRs was investigated by temperature change, and the effect of incorporating cationic ligands on the thermo-responsive properties of cTR-AuNRs was analyzed.

In Chapter 3, my research focuses on exploring whether the cTR-AuNRs can achieve reversible assembly with uniform orientation in polymer brushes. The cTR-AuNRs prepared in Chapter 2 were immobilized in dsDNA brushes by electrostatic interactions. The immobilization state of cTR-AuNRs was evaluated and their thermo-responsiveness in DNA brushes was investigated. In addition, experiments with single-stranded DNA were performed to investigate the generality of the thermo-responsiveness of cTR-AuNRs in polymer brushes. By varying the immobilization density of cTR-AuNRs within the DNA brushes, an understanding of their mobility in polymer brushes was achieved.

In the chapter 4, I summarize the thesis and afford the significance and prospects.

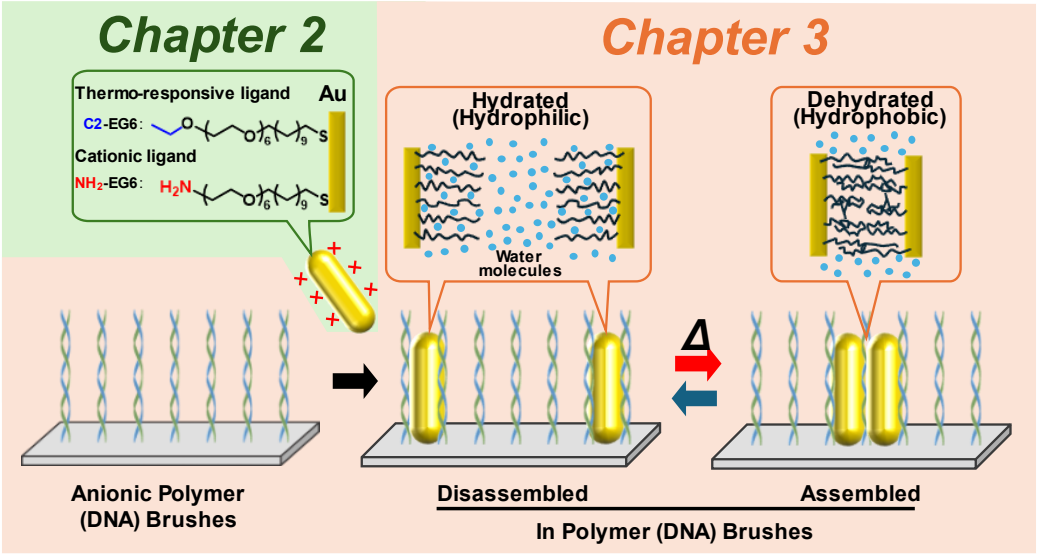


Figure 1-14. Schematic illustration of my doctoral thesis.

Chapter 2

Preparation of Cationic-Thermo-Responsive Gold Nanorods

2-1. Introduction

To attach AuNRs to DNA brushes, the use of cationic ligands is essential.[153] However, it is necessary to investigate whether the incorporation of cationic ligands affects the thermo-responsiveness of thermo-responsive ligand modified AuNRs. In our previous studies, we have shown that AuNRs modified with thermo-responsive ligands exhibit temperature responsiveness in solution.[99,100] In addition, our laboratory has observed that the incorporation of anionic ligands affects the thermo-responsive properties of gold nanodiscs (AuNDs).[102] Therefore, in this chapter, we aim to prepare cation-thermo-responsive AuNRs (cTR-AuNRs) by adjusting the proportion of cationic ligands on the AuNRs surface and to investigate the effect of cationic ligands on the thermo-responsiveness of cTR-AuNRs (Figure 2-1).

The current study delves into the synthesis and comprehensive characterization of cetyltrimethylammonium bromide (CTAB)-coated AuNRs, followed by their functional modification with various ratios of cationic and thermo-responsive ligands. Additionally, the temperature responsiveness of the cTR-AuNRs were investigated. Understanding these properties is crucial for applications that rely on temperature-induced structural change. The study also employs Finite Difference Time Domain (FDTD) simulations to model the assembly process and validate experimental results.

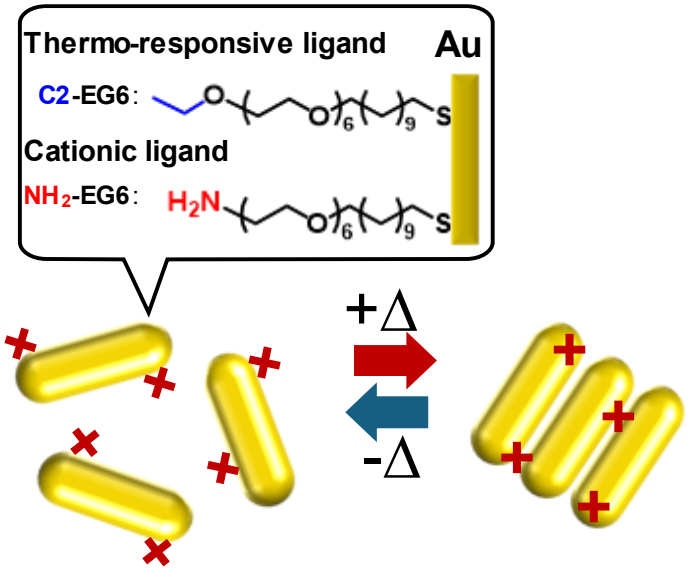


Figure 2-1. Schematic illustration of chapter 2. The cTR-AuNRs reversible assembly in solution.

2-2. Experimental section

2-2-1. Materials and Instruments

Cetyltrimethylammonium bromide (CTAB), ascorbic acid, and silver nitrate were obtained from FUJIFILM Wako Pure Chemical Corporation. $HAuCl_4$-$3H_2O$, L-ascorbic acid, and $NaBH_4$ were purchased from Sigma-Aldrich. ProChimia Surfaces, Sp.zo.o. provided 20-(11-Mercaptoundecanyloxy)-3,6,9,12,15,18-hexaoxaeicosane-1-amine hydrochloride ($NH_2EG_6C_{11}$) and (ethyl-hexa(ethylene glycol)-undecanethiol) ($CH_2CH_3EG_6C_{11}$) (Figure 2-2). All other salts and reagents were purchased from Wako Pure Chemical Industries, Ltd. (Japan) unless otherwise specified. Ultrapure water (18.2 MΩ/cm, Milli-Q, Millipore) was used to prepare all solutions.

The UV-Vis-NIR spectra of the AuNRs were recorded using a JASCO V-770 UV-Vis-NIR spectrophotometer equipped with a PAC-743R automatic 6-position Peltier cell changer. Scanning transmission electron microscopic (STEM) images were obtained using a STEM HD-2000 system (Hitachi High-Tech Manufacturing & Service Co., Ltd., Japan) with a 200 kV acceleration voltage. The zeta-potentials of cationic-thermo-responsive (cTR-) AuNRs were measured with a Zetasizer Nano ZS (Malvern Panalytical Ltd. UK). The buffers used in this study was 5 mM 2-(N-morpholino)ethanesulfonic acid (MES) buffer (pH 6.0).

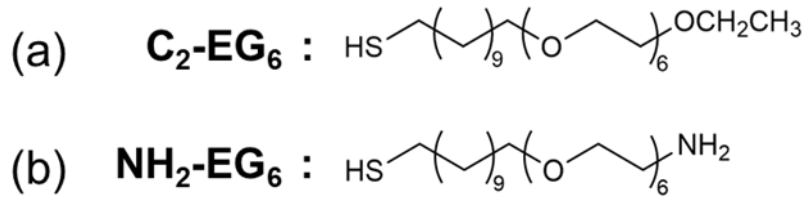


Figure 2-2. Chemical structures of the surface ligands used in this study.
(a) (ethyl-hexa (ethylene glycol)-undecanethiol) ($CH_2CH_3EG_6C_{11}$).
(b) 20-(11-Mercaptoundecanyloxy)-3,6,9,12,15,18-hexaoxaeicosane-1-amine hydrochloride ($NH_2EG_6C_{11}$).

2-2-2. Preparation of AuNRs (36 × 10 nm)

AuNRs (36 × 10 nm) were synthesized using the seed-mediated method with slight modification.[154] Gold seed particles were firstly prepared by a standard reduction process. Under gentle shaking, a 0.01 M ice-cold $NaBH_4$ solution (600 μL) was added to a mixture of a 0.01 M $HAuCl_4 \cdot 3H_2O$ solution (250 μL) and a 0.1 M CTAB solution (7.5 mL). The seed solution was then kept in an incubator (30°C) for 2 h. For the growth reaction, growth solutions were prepared from a 0.1 M CTAB solution (38 mL) by adding a 0.01 M $HAuCl_4 \cdot 3H_2O$ solution (1.6 mL), a 0.01 M $AgNO_3$ solution (240 μL), and an 0.1 M ascorbic acid solution (256 μL), in this order. The gold seed solutions (320 μL) were injected to the growth solutions, while the growth solution was stirred gently. Then, the growth solutions were left undisturbed in an incubator (30°C) for at least 3 h. The AuNR solution was stored under 30°C. For TEM measurement, the remaining CTAB and other reagents were diluted 1000-fold by two-times centrifugation (18,000 g, 20 min, 30°C) before dropping onto a TEM grid.

2-2-3. Quantification of Particle Concentration in AuNRs Dispersions

In the case of AuNRs with a diameter of 10 nm and a length of 36 nm. By simplifying the shape of the gold nanorods to consist of a sphere and a cylinder (Figure 2-3), the volume of a single gold nanorod can be calculated using the following equation.

$$5^2 \times \pi \times 26 + \frac{4}{3}\pi \times 5^3 = 2565.63\ (nm^2)$$

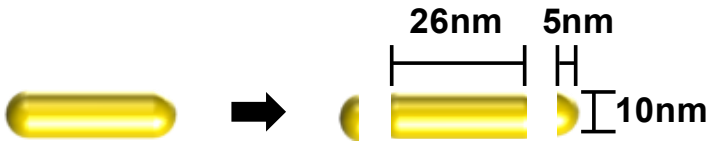


Figure 2-3. Simplification of the shape of AuNRs.

The lattice constant of gold atoms is 4.1×10^{-10} m. The volume occupied by a single gold atom within the AuNR is

$$(\text{Lattice constant})^3 \div 4 = 0.017\ (nm^3)$$

The number of gold atoms constituting a single AuNR is

$$(\text{Single } AuNP \text{ volume}) \div (\text{Single gold atom volume}) = 1.51 \times 10^5$$

The weight of a single AuNR is

$$\frac{\text{Au atomic weight}}{\text{N}_\text{A}} \times (\text{The number of gold atoms constituting a single AuNR})$$

$$= \frac{196.967\ gmol^{-1}}{6.02 \times 10^{23}/mol} \times 1.51 \times 10^5 = 4.94 \times 10^{-17}\ g$$

The concentration of AuNRs in the solution can be determined by the following equation.

$$\text{AuNRs concentration (nM)}$$

$$= \frac{\text{gold atom } concentration(\text{mg/L}) \times \text{Dilution ratio}}{\text{single AuNR mass} \times N_A} \times 10^6$$

2-2-4. Surface modification of AuNRs with two types of thiol-ligands

Different amounts of two kinds of alkanethiol ligands (the $NH_2EG_6C_{11}$ and $CH_3CH_2EG_6C_{11}$ ligands) were mixed in methanol. The ratios of the ligands were 1:99, 5:95, 10:90, 15:85, and 20:80 in a total alkanethiol ligand concentration of 5 mM. Before adding ligand solution to the AuNR solution, the AuNR solution (1 mL) were centrifuged (18,000 g, 20 min, 30°C), and MilliQ-water (940 μL) was added after the supernatant (940 μL) was removed. This centrifugal purification procedure was repeated twice so that the CTAB concentration was approximately 0.36 mM, a concentration suitable for ligand modification. After purification, the mixed ligand solution (50 μL) was added to the purified AuNR solution (950 μL) in a 1.7 mL plastic tube. The AuNR solution with the ligands was vortexed and kept undisturbed at 30°C for at least 24 h. Next, the AuNR solution (1,000 μL) was centrifuged (18,000 g, 20 min, 10°C), the supernatant (950 μL) was removed, and MilliQ-water (950 μL) was added, and the solution was then vortexed. This purification procedure was performed twice. Finally, to obtain a concentrated AuNR solution, the AuNR solution was centrifuged (18,000 g, 20 min, 10°C), and the supernatant (800 μL) was removed.

2-2-5. Evaluation of temperature responsiveness of cTR-AuNRs with different ratio of the cationic ligand

The surface-modified AuNR dispersion (200 μL), 5 mM MES buffer (pH 6.0) (2800 μL) were mixed. The surface charge of the prepared AuNRs was evaluated by zeta potential measurement, and the dispersion state was evaluated by extinction spectrum measurement.

2-2-6. Sigmoidal Curve Fitting for Generalization of AuNR response temperature

The response temperature of cTR-AuNRs was determined from the cooling process by Boltzmann sigmoidal curve fitting of L-LSPR peak shift. Boltzmann sigmoid equation is expressed by:

$$y = \frac{W_{max} - W_{min}}{(1 + e^{(T-T_m)/d})} + W_{min}$$

where y represents the L-LSPR wavelength, T is the temperature, T_m denotes the mid-range of temperature during the disassembly process, that is the response temperature, d signifies the slope factor, and W_{max} and W_{min} represent the maximum and minimum L-LSPR wavelengths.

2-2-7. Time course experiments on assembly/disassembly process

The heating and cooling rate was 1°C min^{-1} for the temperature-change measurements of the AuNRs spectra. The concentrations of AuNRs in solution is 10 nM. For the assembly process, the initial temperature of the AuNRs in solution was maintained at 10°C. Subsequently, the samples were exposed to an environment with a temperature set at 40°C to measure the assembly rate. Conversely, for the dispersion process, the initial temperature of the AuNRs in solution was set at 50°C. The samples were then transferred directly to an environment maintained at 10°C to assess the dispersion rate. Spectral

measurements of these samples were then taken at 10-minute intervals over the next 12 hours.

2-2-8. Evaluation of cTR-AuNRs assembly by Finite Difference Time Domain Method

Finite-difference time-domain (FDTD) simulations were performed to investigate the extinction spectrum of AuNRs using commercial software (Lumerical solutions). All environment of the simulations were set to be water with refractive index of 1.33. The geometric models for the simulation were created according to the experimental structure size of AuNRs. The ligand is ignored in the simulation. In the simulation, I adopted Johnson and Christy dielectric constants for Au.[155] A homogeneous spaced mesh with a mesh size of 1 nm was override the AuNRs.

2-3. Results and Discussion

2-3-1. Evaluation of the shape of CTAB coated AuNRs

The size and shape of the synthesized AuNRs were measured from the STEM image (Figure2-4a). As a result of observing 200 AuNRs, the AuNRs length was 36 ± 3.9 nm and the width was 10 ± 1.8 nm. And 6.0% of quadrangular nanoparticles were present as impurities. In the extinction spectrum of CTAB-coated AuNRs, two plasmon peaks due to the anisotropy of the GNRs were observed (Figure2-4b). From past report, the AuNR has two peaks T-LSPR and L-LSPR.[156,157] These two observed peaks are plasmon peaks peculiar to AuNR. It is also known that the peak of L-LSPR of AuNRs depends on the aspect ratio. The peak wavelength of T-LSPR was 516 nm, and the peak wavelength of L-LSPR was 803 nm. The aspect ratio of the AuNRs obtained this experiment is 3.7,

which is consistent with the past report values indicating this result is a reasonable (Figure 2-5).[157]

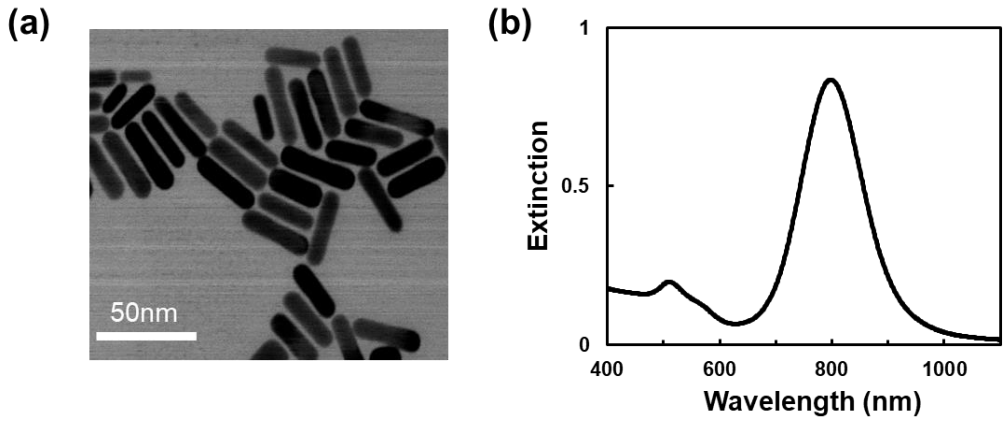


Figure 2-4. STEM image (a) and extinction spectrum (b) of prepared CTA-coated AuNRs. AuNR size was determined as 10 ± 1.8 nm in diameter and 36 ± 3.9 nm in length (200 particles counted).

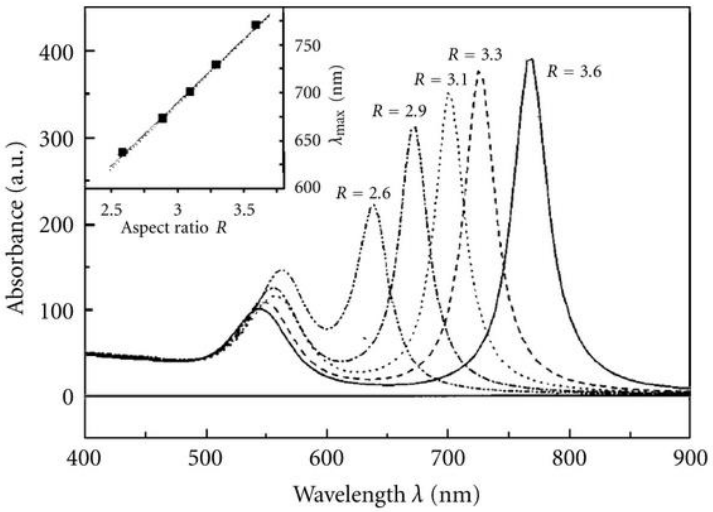


Figure 2-5. Aspect ratio-dependent L-LSPR peak wave of AuNRs.[157]

2-3-2. Evaluation of the modified of cTR-AuNRs with different cationic ligand ratio

The AuNRs modified with mixtures of NH_2- and C2-EG6 ligands were designated as cTR-AuNRs-(X:Y), in which X and Y represent the ligand ratio of NH_2-EG6 to C2-EG6, respectively. Here, cTR-AuNRs-(1:99), -(5:95), -(10:90), -(15:85), and -(20:80) were prepared in a buffer (5 mM MES, pH 6.0) at 10°C. An increase in cationic ligand ratio on the cTR-AuNRs increased the zeta potential, suggesting the successful adjust of cationic ligand by modification (Figure 2-6).

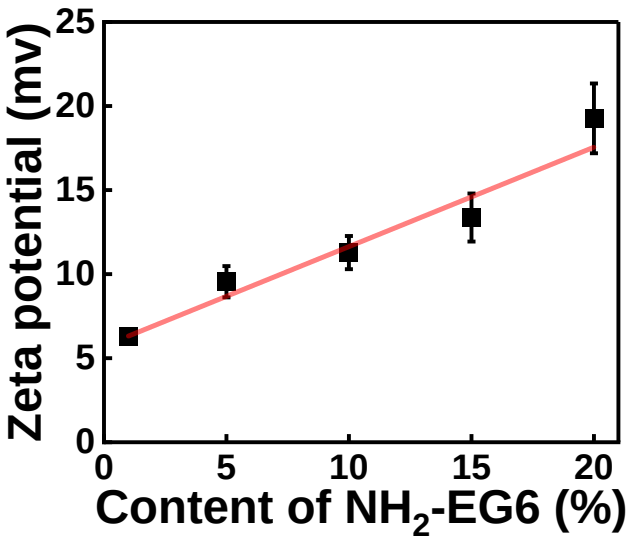


Figure 2-6. Zeta potential of cTR-AuNRs modified with different ratios of NH_2-EG_6 ligands at 10°C in 5 mM MES (pH 6.0). Error bars represent standard deviation (n=3).

2-3-3. Evaluation of temperature responsiveness of cTR-AuNRs with different cationic ligand ratio

From the previous studies, the C2-EG6 ligand modified gold nanoparticles assemble/disassemble in response to temperature, but in this study cation ligand are required for immobilization in DNA brushes. On the other hand, the effect of adding a cationic ligand on temperature responsiveness was unknown. Based on previously reported,[102,158,159] the cationic ligand would influence the responsive temperature of thermo-responsive ligand. Therefore, firstly I investigated about the effect of cationic ligand on temperature responsiveness by observing the changes of L-LSPR of AuNRs modified with different ratios of cationic ligands (prepared in section 2-3-2).

Then, I investigated the thermo-responsiveness of cTR-AuNRs by spectral changes upon heating from 10 to 50°C (Figure 2-7). The cTR-AuNRs-(1:99), -(5:95), -(10:90), -(15:85), and -(20:80) dispersed in solution showed gradual blue shifts of the L-LSPR peak upon heating, indicating side-by-side assembly formation. When the solution was cooled down to 10°C, the L-LSPR peak of all cTR-AuNRs returned to the original position. Figure 2-8 shows the gradual course of the assembly/disassembly of cTR-AuNRs-(10:90) during the heating and cooling process. The temperature was changed between 10 and 50°C at a rate of 1°C/min. Spectral changes were measured every 5°C after 10 min of waiting time. The assembly on heating shows a broad response. On the other hand, on cooling, disassembly occurs within a limited temperature range as a sudden transition. To investigate this hysteresis in the assembly/disassembly of cTR-AuNRs, time-course measurements were performed (Figure 2-9). The assembly of cTR-AuNRs upon heating requires a longer time, over a number of hours, to be equilibrated, while their disassembly upon cooling was completed within 10 minutes, indicating significant time dependence on the assembly formation. Thus, the response temperature of cTR-AuNRs was

determined from the cooling process by Boltzmann sigmoidal curve fitting (prepared in section 2-2-6) of L-LSPR peak shifts (Figure 2-8). The results derived from the curve fitting are summarized in Table 2-1. The response temperatures of cTR-AuNRs-(1:99), -(5:95), -(10:90), -(15:85), and -(20:80) in solution were 12, 19, 22, 25, and 27°C, respectively. These results showed that the response temperature increased with increases in cationic ligand content (Figure 2-10). This trend is consistent with our previous report using anionic ligands.[102] On the other hand, the values of d remained constant within the range between 1.5 and 2.1, regardless of the cationic ligand ratios, indicating that cationic ratio has no significant effect on their sharp responses observed on disassembly.

Next, the reversibility of their assembly/disassembly was confirmed by six cycles of temperature changes between 10 and 50°C (Figure 2-11). The L-LSPR peak of the cTR-AuNRs-(1:99), -(5:95), -(10:90), -(15:85), and -(20:80) showed continuous blue and red shifts with changes in temperature. On the other hand, the degree of peak shifts depended on the cationic ratio, with an increase in the cationic ligand ratio on the cTR-AuNRs resulting in a decrease in L-LSPR peak shifts between 10 and 50°C (Figure 2-12). This phenomenon suggests that electrostatic repulsion interrupts the formation of larger assemblies (explained in section 2-3-4).

These results showed successful preparation of cTR-AuNRs with various cationic charges and significant temperature responsiveness between 10 and 50°C in aqueous solution.

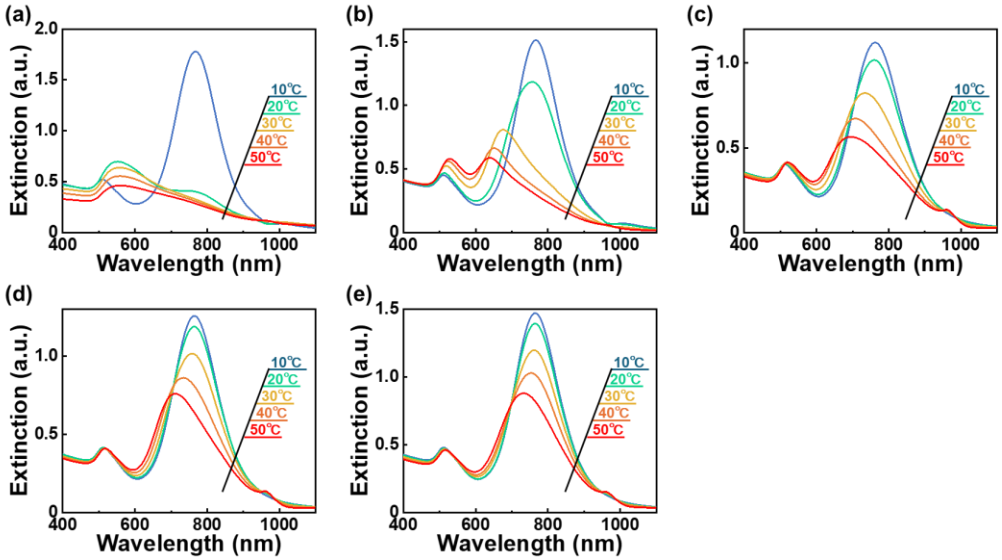


Figure 2-7. Extinction spectra of cTR-AuNRs dispersed in solution with temperature change from 10 to 50°C in solution. (a) cTR-AuNRs-(1:99), (b) cTR-AuNRs-(5:95), (c) cTR-AuNRs-(10:90), (d) cTR-AuNRs-(15:85), and (e) cTR-AuNRs-(20:80).

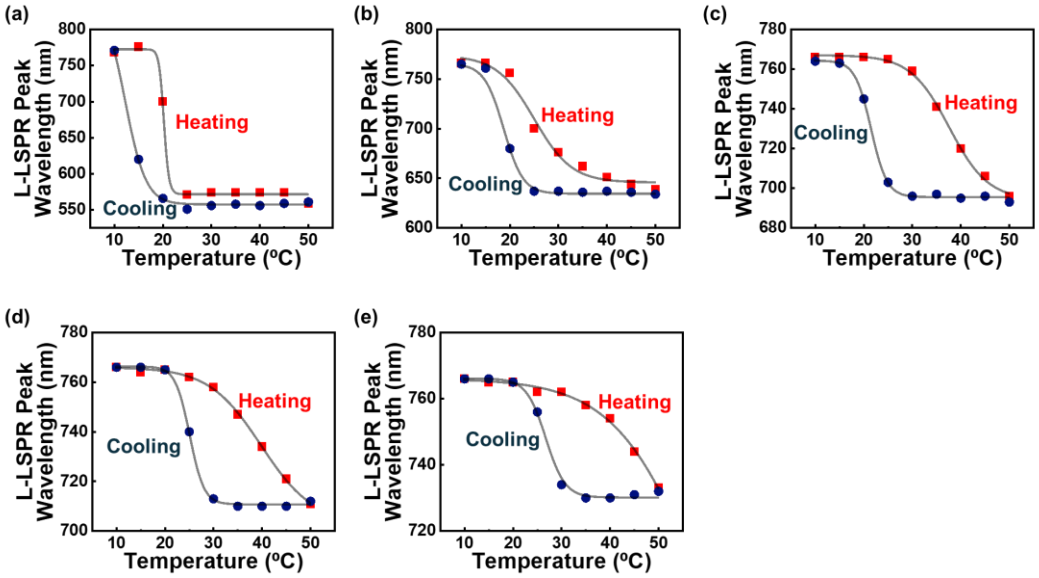


Figure 2-8. L-LSPR peak shift with temperature change in solution on heating (red) and cooling (blue). Gray solid line is curve-fitting. (a) cTR-AuNRs-(1:99), (b) cTR-AuNRs-(5:95), (c) cTR-AuNRs-(10:90), (d) cTR-AuNRs-(15:85), and (e) cTR-AuNRs-(20:80).

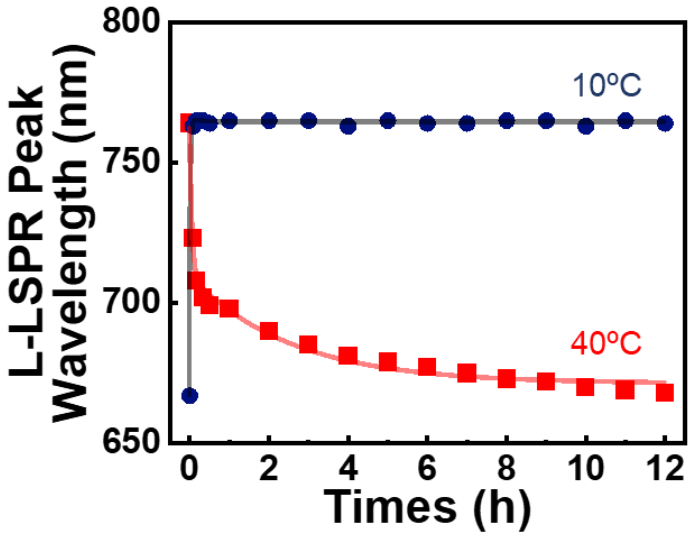


Figure 2-9. The L-LSPR peak shift for cTR-AuNRs-(10:90) over time at 10°C (blue) (initial temperature 50°C) and 40°C (red) (initial temperature 10°C) in 5 mM MES (pH 6.0). The gray solid line is curve fitted from the cooling data. The red solid line is curve fitted from the heating data.

Table 2-1. cTR-AuNRs dispersed in solution upon cooling process curve fitting parameter. Error represents the standard deviation (n=3).

Content of NH_2-EG6 (%)	W_{max} (nm)	W_{min} (nm)	W_{max} -W_{min} (nm)	T_m (°C)	d	R^2
1	771 ± 3	557 ± 2	215 ± 4	12 ± 1.4	2.1 ± 0.4	0.997 ± 0.001
5	765 ± 8	634 ± 3	131 ± 8	19 ± 0.5	2.0 ± 0.4	0.987 ± 0.005
10	764 ± 1	695 ± 1	69 ± 1	22 ± 0.2	1.7 ± 0.1	0.99 ± 0.001
15	766 ± 3	711 ± 1	56 ± 1	25 ± 0.1	1.5 ± 0.2	0.999 ± 0.001
20	766 ± 1	730 ± 1	36 ± 1	27 ± 0.4	2.0 ± 0.3	0.993 ± 0.003

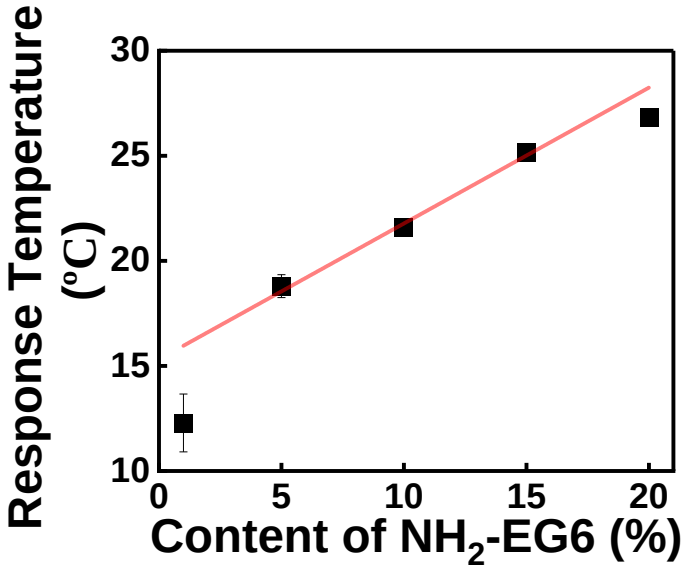


Figure 2-10. Response temperature of cTR-AuNRs modified with different ratios of NH2-EG6 ligands in 5 mM MES (pH 6.0). Error bars represent standard deviation (n=3). The red solid line is a guide for the eye.

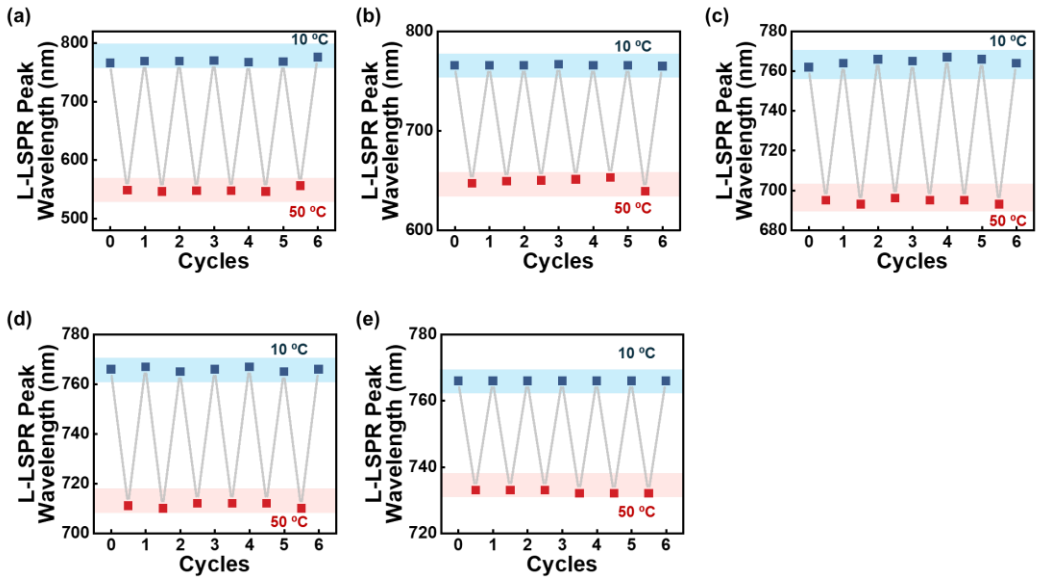


Figure 2-11. L-LSPR peak shift over 6 cycles between 10°C (blue) and 50°C (red). (a) cTR-AuNRs-(1:99), (b) cTR-AuNRs-(5:95), (c) cTR-AuNRs-(10:90), (d) cTR-AuNRs-(15:85), and (e) cTR-AuNRs-(20:80).

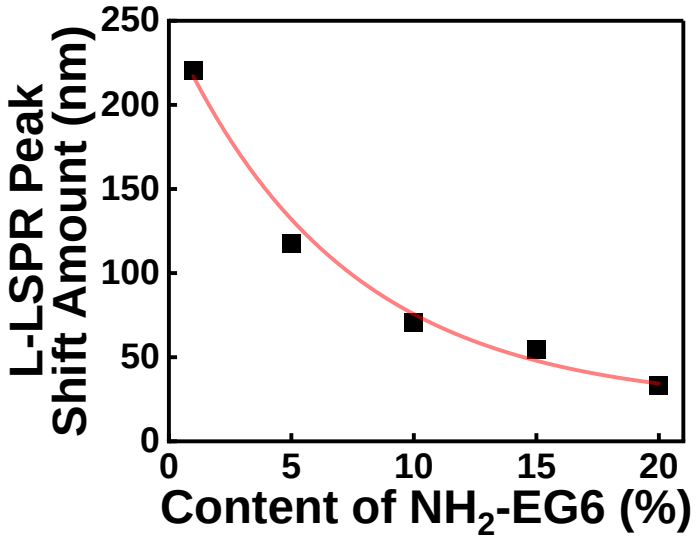


Figure 2-12. The degree of L-LSPR peak shift for cTR-AuNRs modified with different ratios of NH_2-EG6 ligands with temperature change from 10 to 50°C in 5 mM MES (pH 6.0). The red solid line is a guide for the eye.

2-3-4. Evaluation of cTR-AuNRs assembly by Finite Difference Time Domain Method

To investigate the numbers of AuNRs assembly, I use the Finite Difference Time Domain (FDTD) to simulate the AuNRs assembly. Calculated spectra show blue-shifted peaks depending on the number of assemblies. A detailed study of FDTD simulations compared to experimental observations (Figure 2-13). As exemplified by cTR-AuNRs-(1:99), the L-LSPR peak blue shifted to around 560 nm after assembly. From the FDTD results, a nineteen-assembly AuNRs in solution produces an L-LSPR peak at 569 nm that closely matches the experimental result. The cTR-AuNRs-(5:95), -(10:90), -(15:85), and -(20:80) performed a three- to seven-assembly AuNRs, two- to three-assembly AuNRs, two-assembly AuNRs, and one- to two-assembly AuNRs in solution, respectively. In addition, our experimental reveal that the higher cationic ligand ratio, the larger peak wavelength after AuNRs assembled, indicating that the number of AuNRs in the assembly is less (Figure 2-13c). This result supports the hypothesis that repulsion prevents the formation of larger assemblies.

To understand the assembly speed of AuNRs dispersed in solution I use cTR-AuNRs (10:90) as a sample. The results show that two-assembly AuNRs in solution exhibit an L-LSPR peak at 710 nm, which closely matches our experimental results for cTR-AuNRs-(10:90) (Figure 2-9 and Figure 2-13b). Notably, a subsequent blue shift to 668 nm is observed after 12 hours for cTR-AuNRs-(10:90), consistent with the simulated peaks of a three-assembly. This shift indicates a dynamic assembly process that evolves from two to three units, constrained by repulsive forces to stop at a three-assembly.

Through FDTD simulation results, I have effectively elucidated the influence of electrostatic repulsion on the assembly behavior of AuNRs. Furthermore, I have visually represented the assembly process of AuNRs using concrete data.

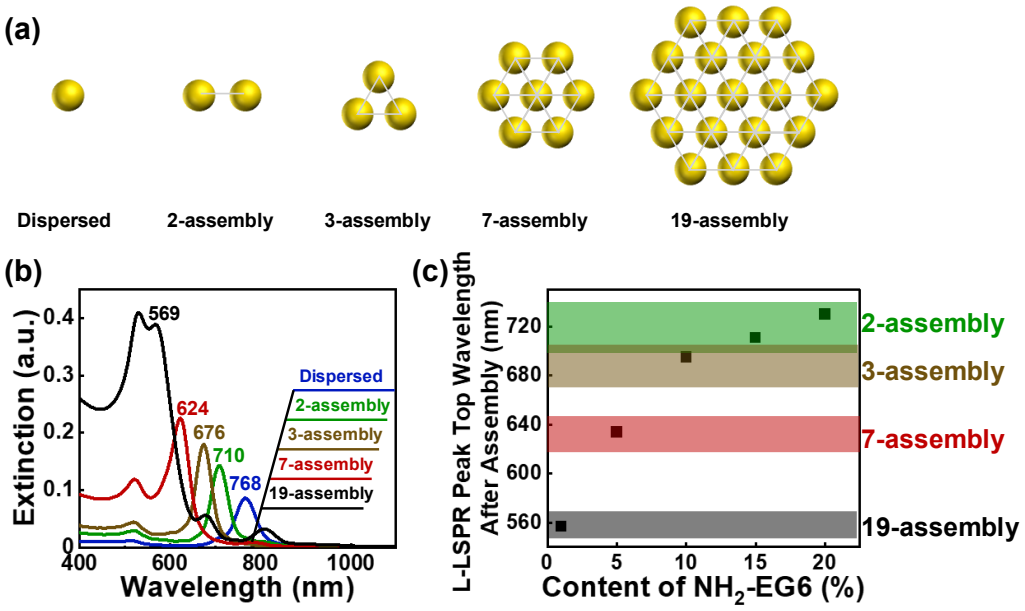


Figure 2-13. (a) Schematic model of the AuNRs disperse in solution; AuNRs assemblies in solution comprising two, three, seven, and nineteen nanorods. AuNRs center-to-center distance is 14 nm. (b) Extinction spectra for AuNRs assemblies calculated by FDTD simulation. The incident light (non-polarized) was used to model the optical properties of single AuNR and small clusters thereof tilted to 45 degrees. (c) The different cationic ratio of cTR-AuNR assembly in experimental corresponding to the number of AuNRs.

2-4. Conclusion

I have successfully prepared the thermo-responsive cTR-AuNRs with different cationic charges. These cTR-AuNRs exhibit significant temperature response in the range of 10 to 50ºC when dispersed in solution. The observed hysteresis during the heating and cooling processes can be attributed to the rapid dispersion kinetics of the AuNRs. Furthermore, the addition of cationic ligands effectively increases the response temperature of the AuNRs and decreases the number of AuNRs involved in the assemblies. These findings highlight the potential of cationic ligands to modulate the thermo-responsiveness of AuNRs, providing valuable insights for the development of advanced nanomaterial systems with controlled assembly and disassembly properties.

Chapter 3

Assembly/disassembly of Cationic-Thermo-Responsive Gold Nanorods in polymer brushes with vertical alignment

3-1. Introduction

In this study, we explore the synthesis and functionalization of AuNRs with cationic and thermo-responsive ligands to prepared cationic-thermo-responsive (cTR-) AuNRs. These AuNRs are then attached to polymer (DNA) brushes to investigate their assembly and disassembly in response to temperature changes. The attachment is driven by electrostatic interactions between the cationic ligands on the cTR-AuNRs and the negatively charged polymer brushes. This approach leverages the unique properties of DNA brushes, which provide a robust and flexible platform for nanomaterial manipulation (Figure 3-1).

The experimental design includes the preparation of DNA brushes, the synthesis of cTR-AuNRs with varying cationic ligand ratios, and the evaluation of their assembly/disassembly using spectra. The use of Finite Difference Time Domain (FDTD) simulations further aids in understanding the assembly dynamics and the role of electrostatic interactions. By varying the cationic ligand ratios and observing the resulting temperature-responsiveness, this study aims to achieve the reversible assembly of cTR-AuNRs in polymer brush substrates.

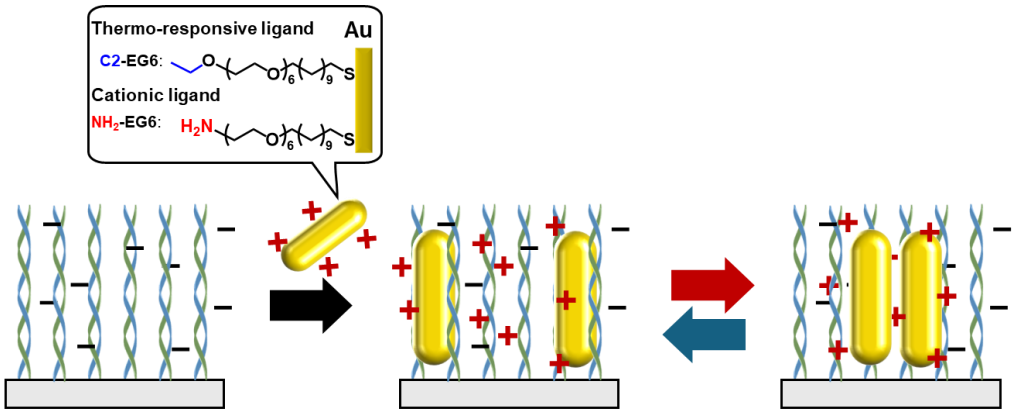


Figure 3-1. Schematic illustration of chapter 3. Preparation of vertical cTR-AuNRs arrays and their reversible assembly by temperature change.

3-2. Experimental section

3-2-1. Materials and Instruments

1-Ethyl-3-(3-dimethylaminopropyl) carbodiimide, hydrochloride (EDC) was purchased from Dojindo Laboratories (Japan). 2-[4-(2-Hydrixyethyl)-1-piperazinyl] ethanesulfonic acid (HEPES) was purchased from Sigma-Aldrich, Inc. (USA). 2-(Carbomethoxy)ethyltrichlorosilane (CMETS) was purchased from Fluorochem, Ltd. (U.K.). Amine-PEG_2-Biotin was purchased from Thermo Fisher Scientific, Inc. (USA). All other salts and reagents were purchased from Wako Pure Chemical Industries, Ltd. (Japan) unless otherwise specified. Ultrapure water (18.2 MΩ/cm, Milli-Q, Millipore) was used to prepare all solutions. Cuvettes with an optical path length of 1 mm were purchased from GL Sciences Inc. Oligonucleotides are purchased from Thermo Fisher Scientific, Inc. (USA) or Integrated DNA Technologies, Inc (USA). The sequences of the oligonucleotide and the chemical structure of the linker between DNA and modification site are shown in Table 3-1.

Table 3-1. Oligonucleotides sequences used in chapter 3.

Description	Sequence (5'→3')
Biotin-Primer	biotin- GAGCCCGTCGCCATCGACTTACG
Alexa647-Primer	Alexa647-GAGCCCGTCGAGAATACTGGC
Biotin-T148	Biotin-T_{148}

λ-DNA was purchased from Nippon Gene Co., Ltd. (Japan). QIA quick PCR Purification Kit was purchased from Qiagen, Inc. (Germany). PCR was performed with

Life Pro thermal cycler (Bioer Technology Co., Ltd). The dsDNA concentration was determined using a Thermo Scientific NanoDrop™ One. Extinction spectra were recorded with a V-730 or V-770 UV-vis spectrometer (JASCO Corp., Japan). The UV-Vis-NIR spectra of the AuNRs were recorded using a JASCO V-770 UV-Vis-NIR spectrophotometer equipped with a PAC-743R automatic 6-position Peltier cell changer. Fluorescence intensity measurements were performed with a Pharos FX Molecular Imager (Bio-Rad Laboratories Inc., USA). The buffers used in this study were as followings; 10 mM Tris(hydroxymethyl)aminomethane (Tris-HCl) buffer (pH 7.6), 10 mM 2-[4-(2-Hydrixyethyl)-1-piperazinyl] ethanesulfonic acid (HEPES-KOH) buffer (pH 8.0), and 5 mM 2-(N-morpholino) ethanesulfonic acid (MES) buffer (pH 6.0).

3-2-2. Synthesis of double-stranded DNA

The DNA for the brushes were synthesized by polymerase chain reaction (PCR) using λDNA as a template. The primers were designed to be 148 base pairs long. To measure the immobilization density, fluorescent dye Alexa647-modified, and biotin-modified DNA were utilized. In a PCR tube, Milli-Q water (44 μL), 2 × Quick Taq HS DyeMix (50 μL), biotin-modified primers (10 μM, 2 μL), Alexa647-modified primers (10 μM, 2 μL), and λDNA (0.20 μg/mL, 2 μL) were added and mixed by pipetting. The PCR solution in the tube was then placed in a thermal cycler. Following the PCR, unreacted primers were removed from the solution using the QIAquick PCR Purification Kit. Initially, 5 equivalents of PB buffer were added and mixed with the solution. The mixture was then placed in a QIAquick column and centrifuged (14,100 g, 60 s, room temperature) to bind the DNA to the column. For purification, 750 μL of PE buffer (provided as an accessory) was added to the column and centrifuged (14,100 g, 60 s, room temperature). Finally, the DNA was recovered by adding 50 μL of Milli-Q water to the column and

centrifuged (14,100 g, 60 s, room temperature) (Figure 3-2). The spectrum of the purified DNA solution was measured using a nanodrop.

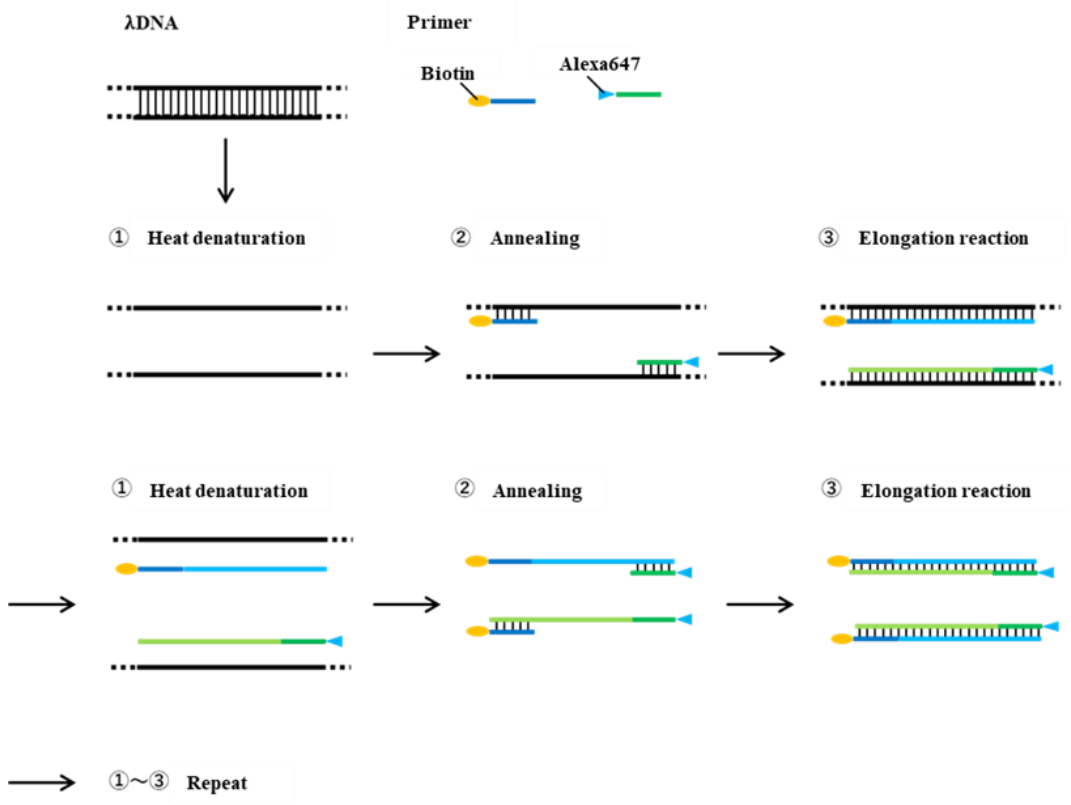


Figure 3-2. Scheme of biotin-modified double-stranded DNA synthesis using PCR reaction.

3-2-3. Preparation of DNA brushes

DNA polymer brushes were prepared according to the previous report (Figure 3-3).[152] The glass substrate was immersed in a Piranha solution (hydrogen peroxide: concentrated sulfuric acid = 3:7) for 1 hour and then dried at 60°C for 2 hours to remove impurities on the substrate. Then, in a nitrogen-filled glove box, 10 mL of toluene, super dehydrated and 3 μL of 2-(carbomethoxy) ethyl trichlorosilane (CMETS) were mixed. Then, A mixture (200 μL) was added to a glass cuvette and stand for 1 hour to provide

methoxycarbonyl group at the glass surface. After, the inside of the glass cuvette was washed with solvents in the order of acetone, ethanol, and Milli-Q water, 400 μL of concentrated hydrochloric acid was added and stand overnight to expose carboxylic acid at the glass surface. Next, 19.2 mg of 1-Ethyl-3-(3-dimethylaminopropyl) carbodiimide Hydrochloride (EDC) was put in a 50 mL tube, 2 mL HEPES-KOH (10 mM, pH 7.6), and 80 μL EZ-Link™ Amine-PEG2-Biotin (50 mM) were added and mixed. Then a mixture (200 μL) was added to a glass cuvette and stand for 1 hour. By this operation, a dehydration condensation reaction was carried out between the carboxylic acid and the amino group at the biotin terminal to prepare a biotin-exposed substrate. After standing for 1 hour, the glass cuvette was washed with Milli-Q water, and 2 mL Tris-HCl (10 mM) and 80 μL streptavidin (5 mg/mL) were mixed, and 200 μL of the mixture was added to a glass cuvette and allowed to stand for 1 hour to prepare a streptavidin-modified substrate. After allowing to stand for 1 hour, a mixture (200 μL) of 10 mM pH 7.6 Tris−HCl buffer containing 200 nM dsDNA (or 2 μM biotin-modified ssDNA) and 1000 mM NaCl was added to a glass cuvette and stand for 2 hours. Then, the glass cuvette was washed with 10 mM Tris-HCl (pH 7.6) to prepare a DNA polymer brush. The dsDNA brushes were evaluated by fluorescence intensity measurement. Using measurements of the average fluorescence intensity across varying concentration gradients of dsDNA (0, 20, 40, 60, 80, and 100 nM) in solution, I have constructed a correlation graph showing the relationship between dsDNA concentration and the corresponding average brightness (Figure 3-4).

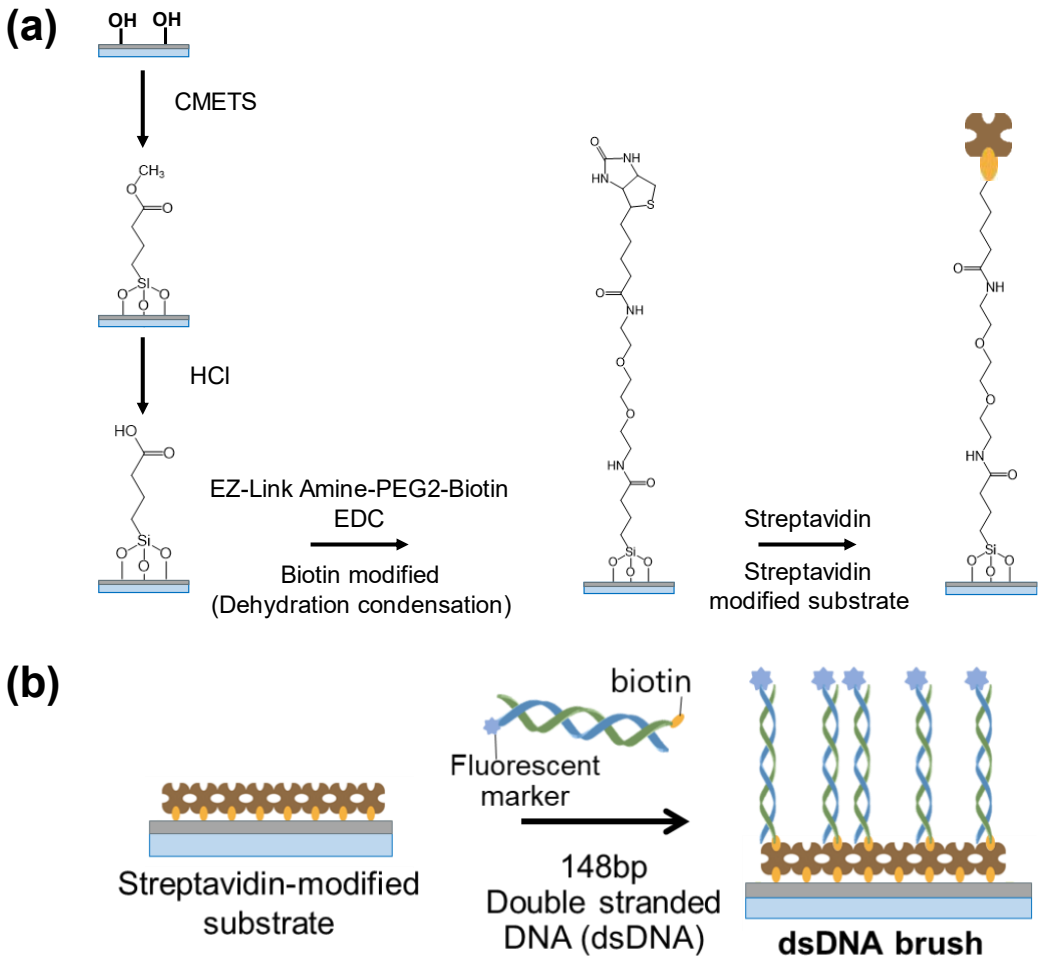


Figure 3-3. Double-stranded DNA polymer brush (a) Streptavidin-modified substrate (b) Double-stranded DNA modified substrate

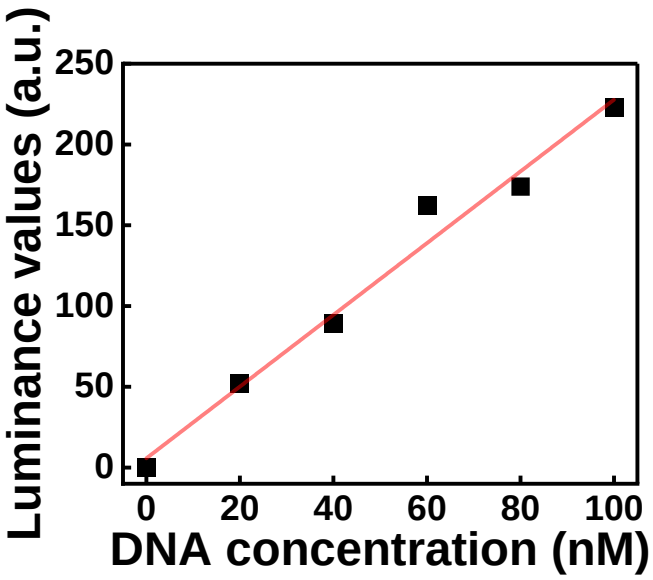


Figure 3-4. Linear plot of mean fluorescence intensity versus DNA concentration of the dsDNA (y = 1.8743x + 0.2857).

3-2-4. Calculation of the DNA density on polymer brushes

The amounts of 148-bp dsDNA on the substrates were calculated from the fluorescence intensities of Alexa 647 modified with the 3' side of ssDNA and the peak absorption intensity at 260 nm. For 148-base ssDNA modified substrates, the peak absorption intensity of DNA at 260 nm was utilized to quantify DNA brush densities. Density evaluation of DNA brushes was performed according to the following calculation formula.

Considering that DNA is immobilized on both sides inside the cuvettes, the relationship between the DNA concentration in the cuvettes and the immobilization density of the DNA polymer brush is as follows:

$$\sigma = \frac{C \times V \times N_A}{S}$$

where σ is DNA immobilization density, C is the DNA concentration in cuvettes, V is the volume of the solution, N_A is the Avogadro constant, and S is surface area of the substrate on which DNA is immobilized.

To calculate the interchain distance of DNA, I assume that the DNA molecules are arranged in a hexagonal close-packed pattern (Figure 3-5). From the estimation, the interchain distance (D_{DNA}) can be calculated by the following formula:

$$D_{\mathrm{DNA}} = \sqrt{\frac{\sqrt{3}}{\sigma \times 2}}$$

From the above calculations, the density of DNA brushes and the distance between DNAs were obtained.

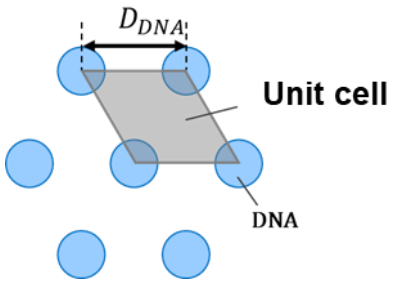


Figure 3-5. Scheme of distance between DNA strands $\boldsymbol{D_{DNA}}$ and unit cell assuming that DNA is arranged in a hexagonal close-packed pattern.

3-2-5. Calculation of the AuNRs attachment density on polymer brushes

The amount of the adsorbed AuNRs was measured using UV-vis-NIR spectroscope by subtracting the amount of the non-adsorbed AuNRs from the added amount of the AuNRs.[153] The AuNRs attachment density can be calculated by the extinction on 400nm (Figure 3-6).

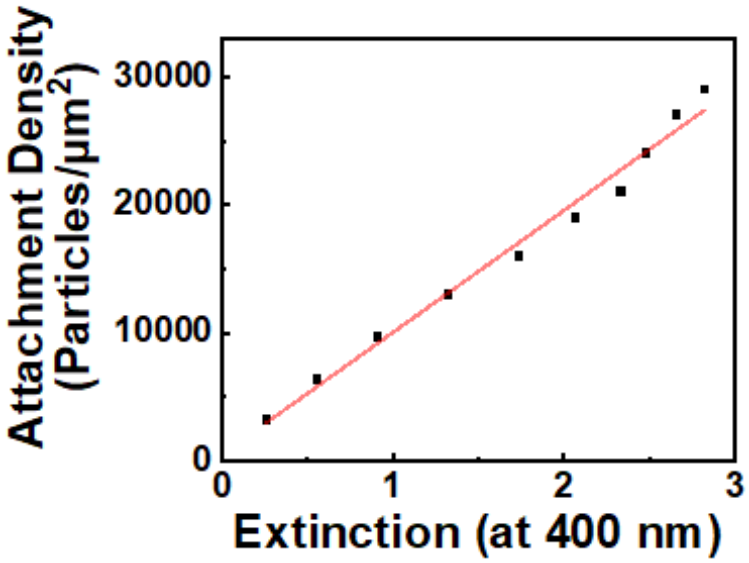


Figure 3-6. The relationship between the AuNRs attachment density in the 148 bp dsDNA brush and the AuNRs extinction at 400nm after attaching in DNA brushes. (y = 9718.5x).[153]

3-2-6. Surface modification of AuNRs with two types of thiol-ligands

Surface modification of the cationic-thermo-responsive (cTR-) AuNR variants was conducted as described in Chapter 2 (2-2-3).

3-2-7. Attachment of cTR-AuNRs into DNA polymer brushes

The prepared cTR-AuNRs were attached to the DNA brush, which is fabricated inside of the cuvettes, by soaking 200 μL of AuNR solution (6.6, 19.8, 33, 66, and 99 nM) for 10 minutes. After that, the inside surface of the cuvette was washed with 5 mM MES (pH 6.0) at least three times to remove the nonattached cTR-AuNRs.

3-2-8. Baseline of the p- and s-polarization

For the establishment of baselines, I meticulously measured spectra of the water samples with the cuvettes, featuring an optical path length of 1 mm, under both p-polarized and s-polarized light conditions.

3-2-9. Sigmoidal Curve Fitting for Generalization of AuNR response temperature

Evaluation of the cTR-AuNRs response temperature was conducted as described in Chapter 2 (2-2-5).

3-2-10. Evaluation of cTR-AuNRs orientation and assembly into DNA polymer brushes by Finite Difference Time Domain Method

Finite-difference time-domain (FDTD) simulations were performed to investigate the extinction spectrum of AuNRs using commercial software (Lumerical solutions). All environment of the simulations were set to be water with refractive index of 1.33. The geometric models for the simulation were created according to the experimental structure size of AuNRs. The ligand is ignored in the simulation. In the simulation, I adopted Johnson and Christy dielectric constants for Au.[155] A homogeneous spaced mesh with a mesh size of 1 nm was override the AuNRs. For the simulation of tilted AuNRs, Bloch Boundary Conditions were set up to apply a phase correction to the fields.

3-2-11. Time course experiments on assembly/disassembly process

The heating and cooling rate was 1°C min^{-1} for the temperature-change measurements of the AuNRs spectra. The initial temperature of the AuNRs in solution was maintained at 10°C. Subsequently, the samples were exposed to an environment with a temperature set at 30°C to measure the assembly rate. Conversely, for the dispersion process, the initial temperature of the AuNRs in solution was set at 50°C. The samples were then transferred directly to an environment maintained at 10°C to assess the dispersion rate. Spectral measurements of these samples were then taken at 10-minute intervals over the next 1 hours.

3-3. Results and discussion

3-3-1. Synthesis of double-stranded DNA

The number of base pairs and the concentration of the double-stranded DNA prepared in Section 3-2-2 were evaluated. The number of base pairs was evaluated by agarose gel electrophoresis, and the concentration was evaluated by absorption spectrum measurement. The results of agarose gel electrophoresis show that a band exists near 150 bp when compared with the marker (Figure 3-7a). Since the number of base sequences of the target DNA was designed to be 148 bp (length is 50nm), it was found that a double-stranded DNA of an appropriate length was prepared. In the absorption spectrum of the double-stranded DNA sample, the absorption intensity at 260 nm, which is the absorption peak of the double-stranded DNA, was 5.96 (Figure 3-7b). Assuming that all these double-stranded DNAs were 148 bp, the concentration of double-stranded DNA was calculated to be 2.85 μM. The value obtained by dividing the absorption intensity at 260 nm by the absorption intensity at 280 nm was 1.9. A260/A280 between 1.5 and 2.0 is considered appropriate to be a pure DNA.[160] From the above, I got a pure 148bp DNA.

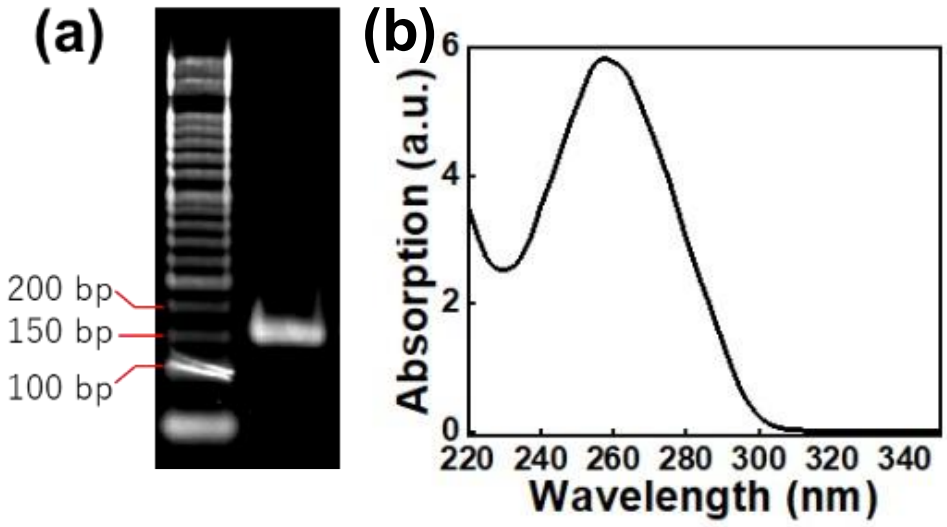


Figure 3-7. (a) Agarose gel electrophoresis image of the sample after PCR. Left lane: marker, right lane: sample after PCR. (b)Absorption spectrum of 148-bp dsDNA after PCR.

3-3-2. Evaluation of double-stranded DNA polymer brushes on substrates

The density of the double-stranded (ds) DNA polymer brush prepared in Section 3-2-3 was evaluated by fluorescence intensity measurement. Fluorescence intensity measurements showed a density of 18,000 ± 2,300 (chains / μm^2) and an interchain distance of 7.9 ± 0.5 nm. In addition, uniform fluorescence intensity was confirmed in the area containing the DNA solution (Figure 3-8). In previous studies, the DNA distance was 7.0 ± 0.2 nm.[153] It indicates that the double-stranded DNA polymer brush was properly prepared in this study.

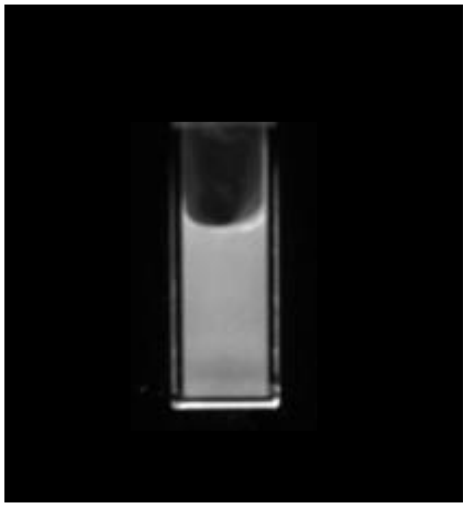


Figure 3-8. Fluorescence image of the dsDNA brush. The density of DNA molecules within the brushes was determined to be approximately 18,000 ± 2,300 strands per square micrometer (with an average DNA interchain distance of 7.9 ± 0.5 nm).

3-3-3. Evaluation of attachment of cTR-AuNRs with different cationic ligand ratio into double-stranded DNA polymer brushes

To immobilize cTR-AuNRs in DNA brushes with vertical orientation via electrostatic interactions, cTR-AuNRs with different cationic ligand ratios were applied to DNA brushes. dsDNA brushes were prepared in Section 3-2-3. The cTR-AuNRs were attached in DNA brushes through electrostatic interactions at 10°C. After 10 minutes, the unabsorbed AuNRs in the bulk solution were removed by replacement of the buffer (5 mM MES, pH 6.0) 3 times. Their attachment to DNA brushes was evaluated by spectral analyses (Figure 3-9).

I first evaluated the attachment density of cTR-AuNRs in DNA brushes from extinction spectra under the incident light perpendicular to the substrate (Figure 3-10). The quantitative assessment of adsorbed cTR-AuNRs was calculated from the extinction at 400 nm.[152] The cTR-AuNRs-(1:99), -(5:95), -(10:90), -(15:85), and -(20:80) respective adsorption densities were quantified as 600, 900, 1050, 1100, and 1100 particles/μm²,

respectively. Correspondingly, these adsorption densities were translated into average center-to-center distances between the adsorbed cTR-AuNRs, which were calculated to be approximately 44, 36, 33, 32, and 32 nm, respectively.

Next, their orientation was evaluated by extinction spectrum under the incident light perpendicular to the substrate. cTR-AuNRs-(1:99) and -(5:95) exhibited a pronounced strong L-LSPR intensity at around 770 nm, which significantly exceeds that of the transverse localized surface plasmon resonance (T-LSPR) at around 520 nm. In contrast, compared with the extinction spectra of cTR-AuNRs dispersed in solution, cTR-AuNRs-(10:90), -(15:85), and -(20:80) immobilized in DNA brushes exhibited a distinctly weak L-LSPR intensity, which is significantly lower than that of the T-LSPR. As well known, the L-LSPR extinction shows significant dependence on the angle of the incident light to AuNRs, while the T-LSPR does not.[137] Therefore, the intensity of the L-LSPR peak at a longer wavelength divided by that of the T-LSPR peak at a shorter one (L-/T-LSPR) can be an indicator of the AuNR orientation.[152] cTR-AuNRs-(1:99) and -(5:95) showed a high L-/T-LSPR intensity (3.4 and 1.9). The cTR-AuNRs -(10:90), -(15:85), and -(20:80) had a low L-/T-LSPR intensity (0.4). In the analogous system, side-by-side plasmon coupling was facilitated on vertically aligned AuNR arrays, while tilting of AuNRs by environmental manipulation resulted in the elimination of that side-by-side coupling due to their random orientation.[161] Numerically, this phenomenon corresponds to an L-/T-LSPR ratio less than 1.0, indicating a vertical arrangement of AuNRs. To estimate the tilt angle of AuNRs with an L-/T-LSPR value, finite-difference time-domain (FDTD) simulations were performed with single AuNRs, thereby eliminating the influence of plasmon coupling caused by side-by-side alignment of vertically oriented AuNRs (Figure 3-11a, b). The FDTD simulation suggests AuNR arrays with an L-/T-LSPR value of 1.0

have approximately 10 degrees of the tilt angle to the vertical, which is regarded to be perpendicular to the substrate. Based on the low L-/T-LSPR values less than 1.0, we concluded cTR-AuNRs-(10:90), -(15:85), and -(20:80) were vertically aligned in the dsDNA brushes (Figure 3-11c).

To directly observe L-LSPR in vertically aligned AuNRs, we tilted the substrate at 45 degrees and then observed the extinction spectra under p- and s-polarized light (Figure 3-12). For cTR-AuNRs-(10:90), -(15:85), and -(20:80), a new peak was observed at around 630 nm only under p-polarized light (Figure 3-13c-e). This p-polarized light specific peak results from L-LSPR of vertically aligned AuNRs as the side-by-side plasmon coupling.[161] On the other hand, cTR-AuNRs-(1:99) and -(5:95) attached on dsDNA brushes did not show any new peak in extinction spectra under p-polarized light compared to those under s-polarized (Figure 3-13a, b). The extinction spectra under polarized light provide robust evidence for the vertical alignment of cTR-AuNRs-(10:90), -(15:85), and -(20:80) in dsDNA brushes. This observation also supports our estimation of the attachment density of cTR-AuNRs-(10:90), (15:85), and (20:80). From the blue shifts of this distinct peak by side-by-side plasmon coupling under p-polarization, their center-to-center distances were estimated to be 28, 29, and 29 nm from the FDTD simulation in our previous study,[152] which show good agreement with those calculated from the extinction at 400 nm.

These results verified that cTR-AuNRs-(10:90), -(15:85), and -(20:80) were vertically attached in dsDNA brushes under the controlled electrostatic interaction.

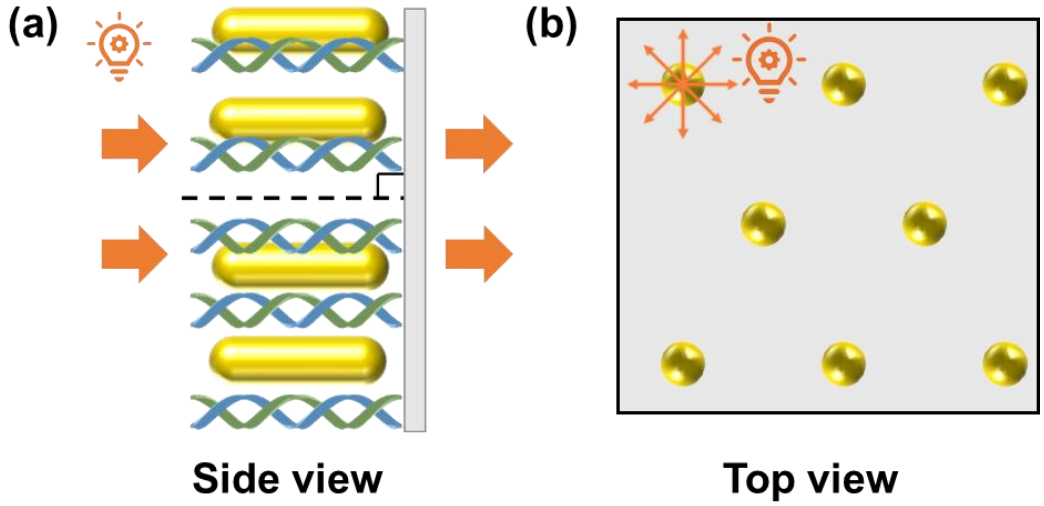


Figure 3-9. Schematic illustration of cTR-AuNRs in dsDNA brushes under incident light (non-polarized) perpendicular to the substrate. (a) Side view. (b) Top view.

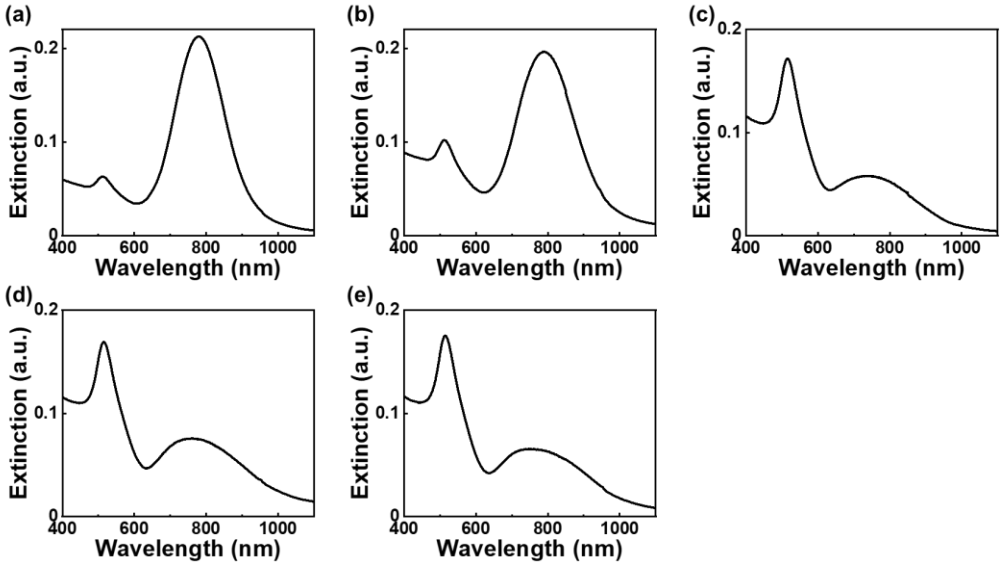


Figure 3-10. Extinction spectra of cTR-AuNRs attached in dsDNA brushes at 10°C. (a) cTR-AuNRs-(1:99), (b) cTR-AuNRs-(5:95), (c) cTR-AuNRs-(10:90), (d) cTR-AuNRs-(15:85), and (e) cTR-AuNRs-(20:80).

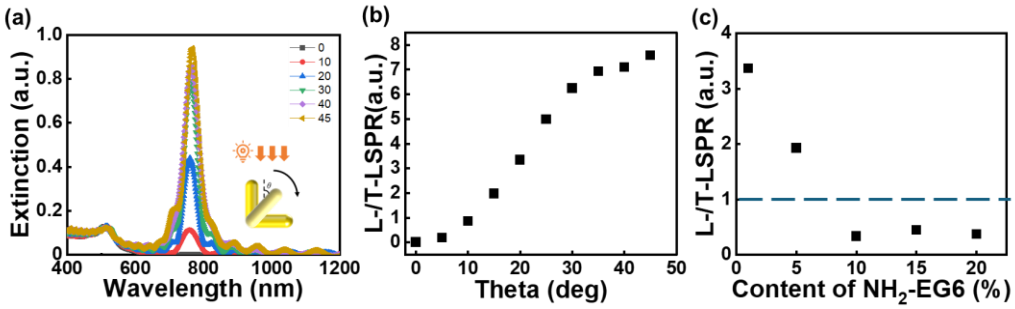


Figure 3-11. (a) Simulated extinction spectra of AuNRs in different orientations under circularly polarized light. (b) The relationship graph between L-/T-LSPR and theta obtained from FDTD simulations. (c) L-/T-LSPR of cTR-AuNRs modified with different ratios of NH_2-EG6 ligand which attached in dsDNA brushes. The dashed line is a guideline for the L-/T-LSPR equal to 1.0.

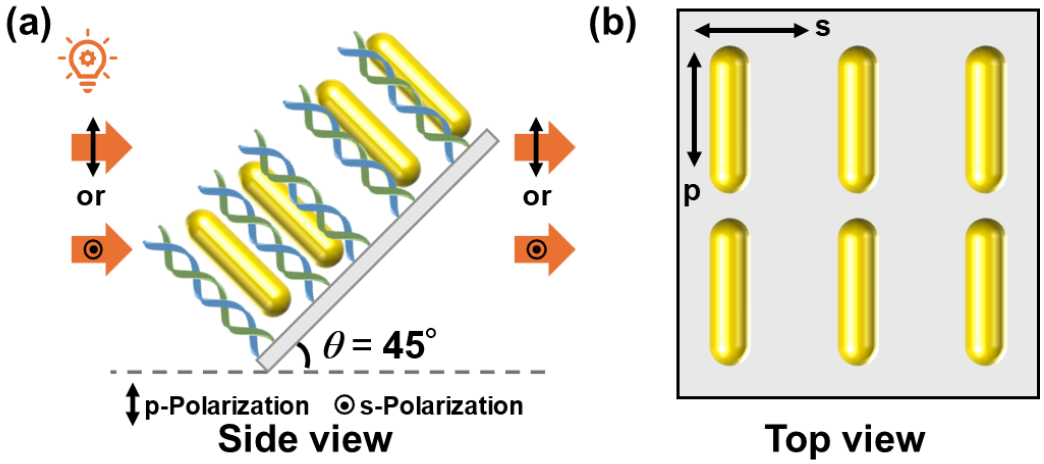


Figure 3-12. Schematic illustration of cTR-AuNRs in dsDNA brushes under p- and s-polarized light with the substrate tilted at 45 degrees. (a) Side view. (b) Top view.

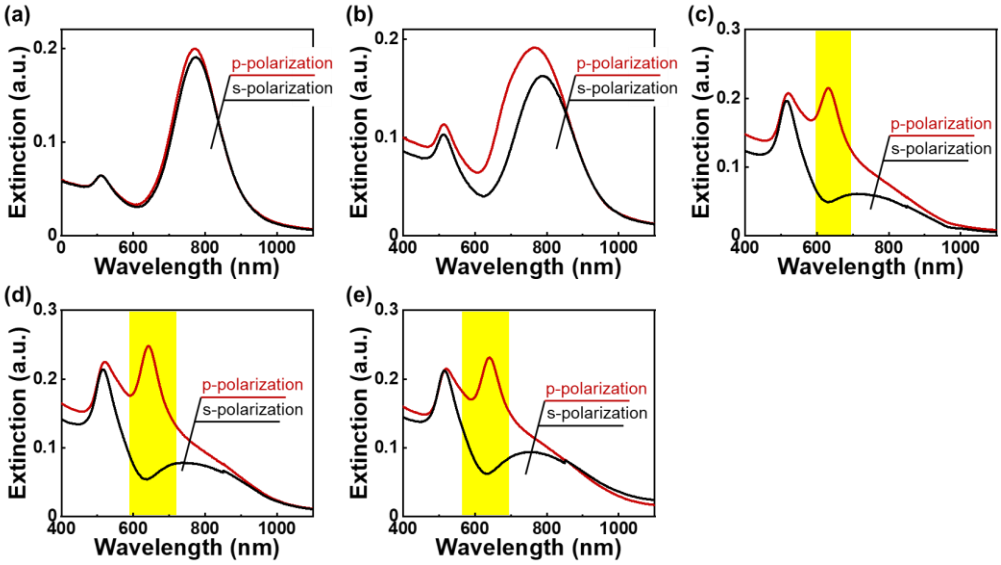


Figure 3-13. Extinction spectra of cTR-AuNRs attached in dsDNA brushes under p- (red) and s-polarized light (black) at 10°C. (a) cTR-AuNRs-(1:99), (b) cTR-AuNRs-(5:95), (c) cTR-AuNRs-(10:90), (d) cTR-AuNRs-(15:85), and (e) cTR-AuNRs-(20:80).

3-3-4. Evaluation of cTR-AuNRs reversible assembly change on double-stranded DNA polymer brushes by temperature change

To investigate the thermo-responsive assembly of cTR-AuNRs with uniform orientation, cTR-AuNRs-(10:90), -(15:85), and -(20:80) immobilized in dsDNA brushes were heated. Next, the extinction spectra of cTR-AuNRs were measured under the incident light perpendicular to the substrate at 50°C (Figure 3-14). The consistent absorbance observed at 400 nm indicates that the AuNRs remained firmly anchored within the brush matrix despite the thermally induced assembly/disassembly processes, with no evidence of detachment observed.

The extinction spectra of cTR-AuNRs were measured under p- and s-polarization at 50°C (Figure 3-15). The p-polarization-specific peak for cTR-AuNRs at around 600 nm showed that the cTR-AuNRs were vertically aligned in the dsDNA brushes after heating. The specific peak for cTR-AuNRs on L-LSPR almost merged with the T-LSPR peak, making analyses of the L-LSPR peak complex. Fortunately, as vertically aligned AuNR arrays show a p-polarized light-specific L-LSPR peak that is not observed under s-polarization, we could eliminate the other peaks (i.e., those for T-LSPR at around 530 nm and L-LSPR at around 770 nm) for AuNRs out of the vertical alignment, by subtracting the s-polarized extinction spectra from the p-polarized spectra as the differential spectra (Figure 3-16). The differential spectra at 10 and 50°C clearly show a blue shift in L-LSPR upon heating, suggesting that the cTR-AuNRs are assembled in a side-by-side manner (Figure 3-17).

Next, we gradually decreased the temperature from 50 to 10°C (Figure 3-18). The data derived from the curve fitting are summarized in Table 3-2. The average response temperatures of cTR-AuNRs-(10:90), -(15:85), and -(20:80) in the DNA brushes were 24, 29, and 32°C, respectively. An increase in the cationic ligand content caused an increase

in the response temperature (Figure 3-19). This trend is consistent with that observed for AuNRs dispersed in solution. Upon subsequent cooling of the substrate after heating, the L-LSPR of the cTR-AuNRs returned to its original state, underscoring the clear reversibility of this dynamic change. The peak shift trend observed for cTR-AuNRs-(10:90), -(15:85), and -(20:80) in the dsDNA brushes was also consistent with their behavior dispersed in solution, although their degree of shift was smaller than when dispersed in solution (Figure 3-20). The center-to-center distance of the AuNRs dispersed in solution and immobilized in the DNA brushes was calculated to be about 55 μm and 30 nm, respectively, based on the solution concentration and extinction at 400 nm. Consequently, the initial distance between the AuNRs is considered to influence the plasmon coupling shift. In addition, the assembly size, which is defined by the number of AuNRs that make up the assembly, may also contribute to this phenomenon. The underlying causes for this reduction in the degree of shift is discussed below. The assembly/disassembly phenomenon exhibits good repeatability (Figure 3-21).

It is also noticeable that the cTR-AuNRs in DNA brushes showed faster assembly/disassembly kinetics than did those dispersed in solution, although less mobility was expected due to their interaction with the DNAs (Figure 3-22). Their assembly was mostly completed within 10 minutes of heating, while the disassembly process upon cooling was completed within 5 minutes. As the AuNRs exist in a thin layer of less than 50 nm, the shorter distances between AuNRs, the limited space for their movement, and the limited variation in orientation may accelerate their assembly in a side-by-side manner, which could be the reason for the faster assembly/disassembly in the dsDNA brushes. The limitations associated with their existence in a thin layer, such as space and orientation, could lead to a more efficient reaction, in this case, assembly formation, in the same

manner as cell membranes in living bodies. Although their movement velocity in the DNA brushes remains unclear, the quick disassembly process supports the notice that they have good mobility even when immobilized in DNA brushes.

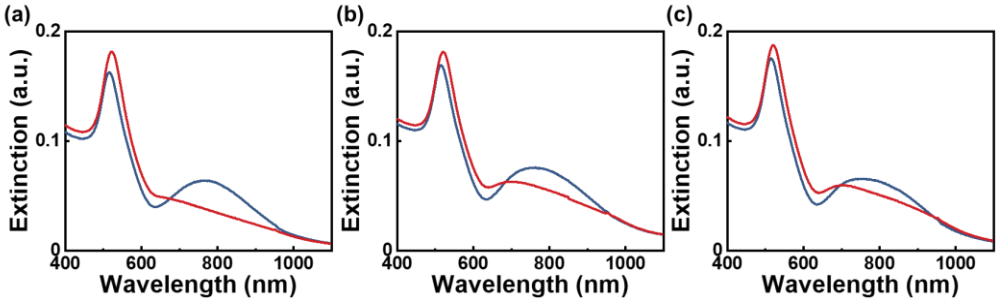


Figure 3-14. Extinction spectra of cTR-AuNRs in dsDNA brushes under incident light (non-polarized) perpendicular to the substrate at 10°C (blue) and 50°C (red). (a) cTR-AuNRs-(10:90), (b) cTR-AuNRs-(15:85), and (c) cTR-AuNRs-(20:80).

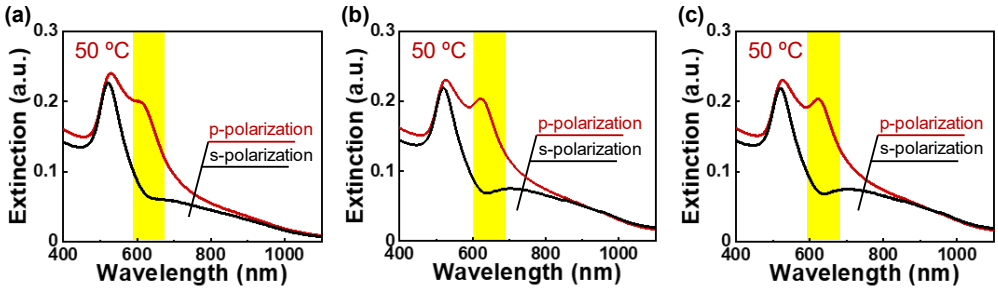


Figure 3-15. Extinction spectra of cTR-AuNRs attached in dsDNA brushes under p- (red) and s-polarized light (black) at 50°C. (a) cTR-AuNRs-(10:90), (b) cTR-AuNRs-(15:85), and (c) cTR-AuNRs-(20:80).

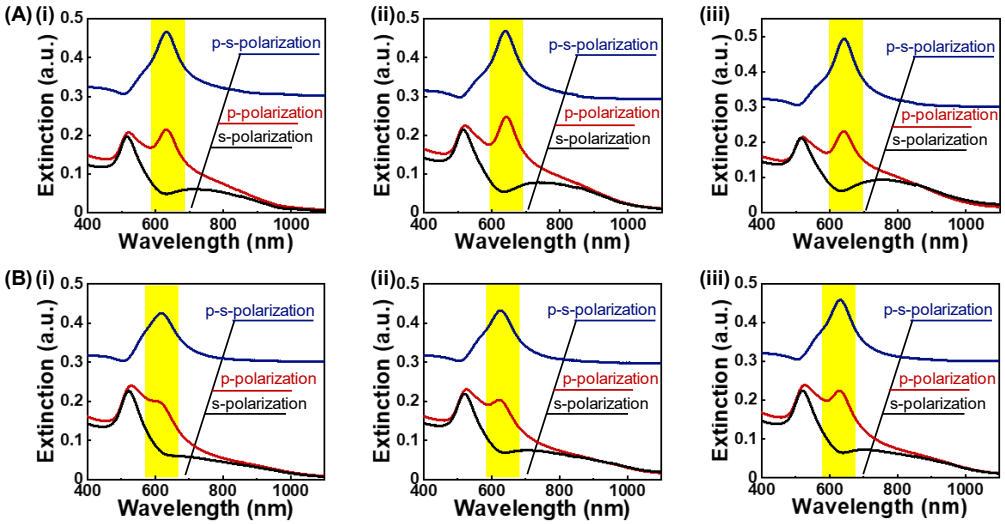


Figure 3-16. Extinction spectra of cTR-AuNRs attached in dsDNA brushes under p- (red), s-polarized light (black), and difference extinction spectrum of p- and s-polarized light (blue) at (A) 10°C and (B) 50°C. (i) cTR-AuNRs-(10:90), (ii) cTR-AuNRs-(15:85), and (iii) cTR-AuNRs-(20:80).

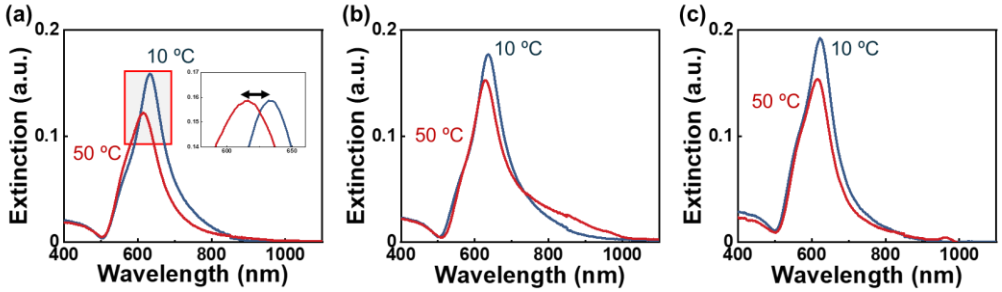


Figure 3-17. The difference extinction spectrum under p- and s-polarized light at 10°C (blue) and 50°C (red). (a) cTR-AuNRs-(10:90), (b) cTR-AuNRs-(15:85), and (c) cTR-AuNRs-(20:80). Inset is the magnified view of the normalized L-LSPR peaks at each temperature.

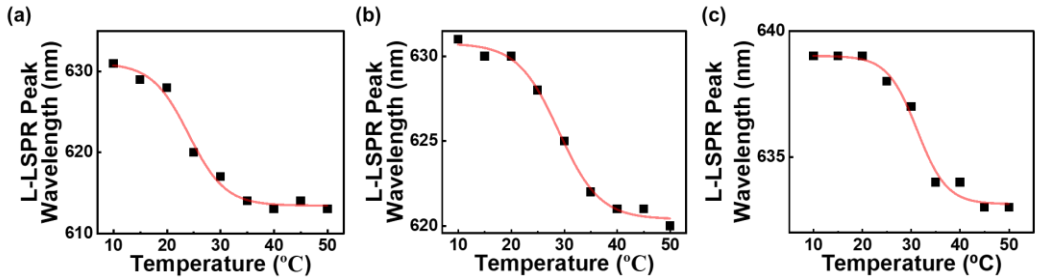


Figure 3-18. L-LSPR peak shift upon cooling process (from 50 to 10°C) extracted from difference extinction spectrum of p- and s-polarized light in the dsDNA brush. (a) cTR-AuNRs-(10:90), (b) cTR-AuNRs-(15:85), and (c) cTR-AuNRs-(20:80).

Table 3-2. cTR-AuNRs immobilized in dsDNA brushes upon cooling process curve fitting parameter. Error represents the standard deviation (n=3).

Content of NH_2-EG6 (%)	W_{max} (nm)	W_{min} (nm)	W_{max} -W_{min} (nm)	T_m (°C)	d	R^2
10	631 ± 1	613 ± 1	18 ± 1	24 ± 0.8	3.4 ± 0.7	0.983 ± 0.007
15	631 ± 1	620 ± 1	11 ± 1	29 ± 0.6	3.9 ± 0.7	0.992 ± 0.003
20	639 ± 1	633 ± 1	6 ± 1	32 ± 0.8	3.0 ± 0.7	0.977 ± 0.008

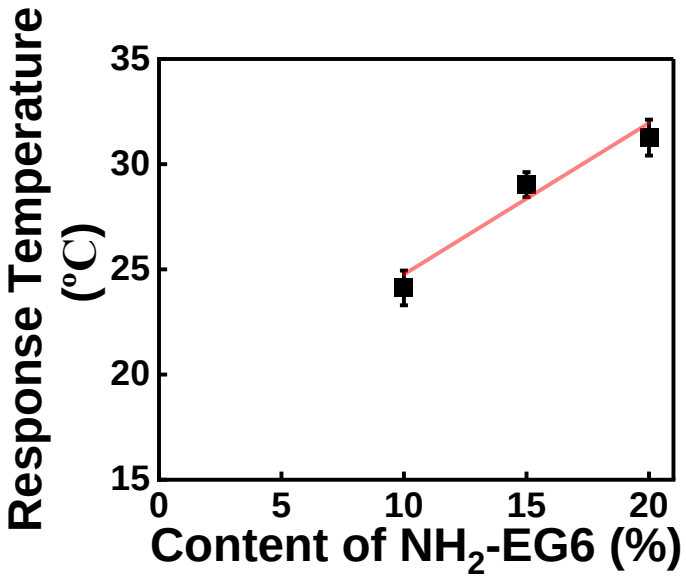


Figure 3-19. Response temperature of cTR-AuNRs modified with different ratios of NH_2-EG6 ligands in dsDNA brushes. The red solid lines are guides for the eye. Error bars represent standard deviation (n=3).

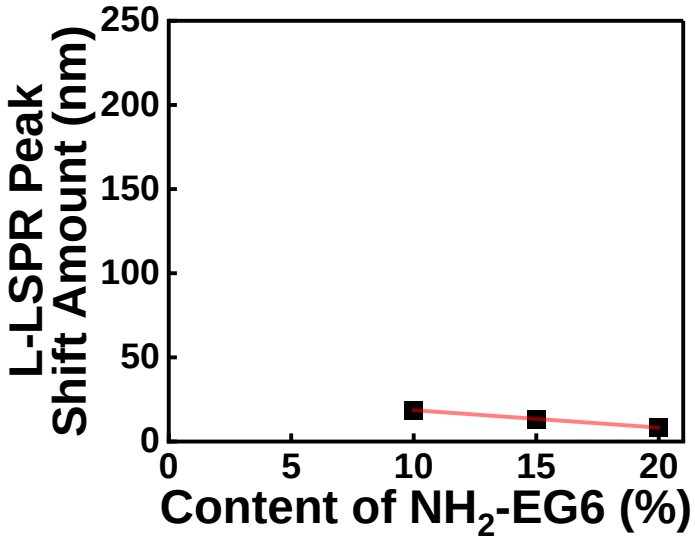


Figure 3-20. L-LSPR peak shift of cTR-AuNRs modified with different ratios of NH_2-EG6 ligands with temperature change in dsDNA brushes. The red solid lines are guides for the eye. Error bars represent standard deviation (n=3).

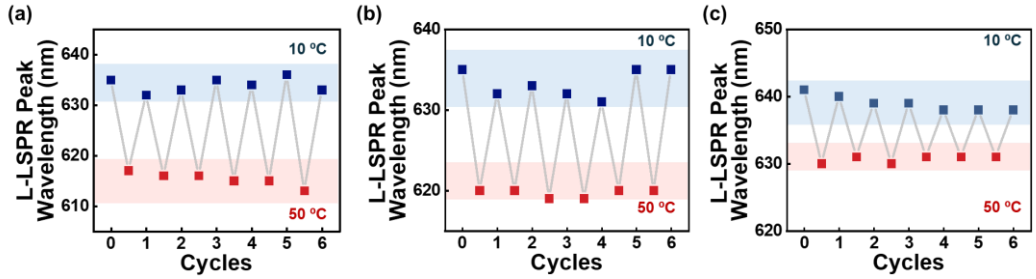


Figure 3-21. L-LSPR peak shift in the difference extinction spectrum in 6 cycles between 10°C (blue) and 50°C (red). (a) cTR-AuNRs-(10:90), (b) cTR-AuNRs-(15:85), and (c) cTR-AuNRs-(20:80).

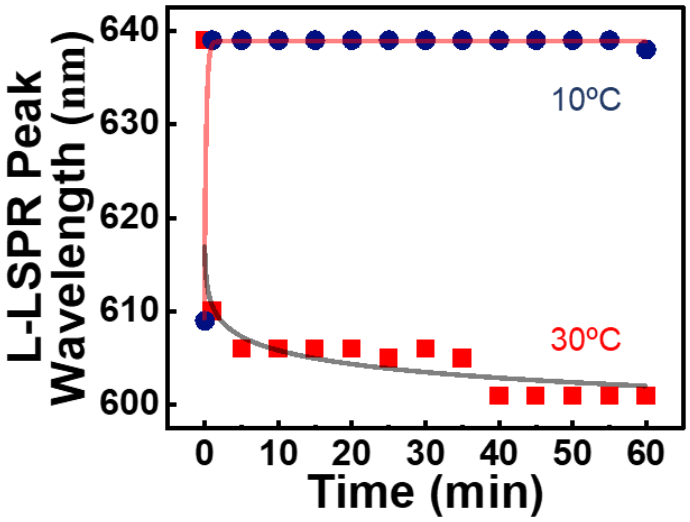


Figure 3-22. L-LSPR peak shift of cTR-AuNRs-(10:90) under p-polarization over time at 10°C (blue) (initial temperature 50°C) and 30°C (red) (initial temperature 10°C) in dsDNA brushes. Gray solid line is curve fitted from the heating data. Red solid line is curve fitted from the cooling data.

3-3-5. Evaluation of cTR-AuNRs reversible assembly change on single-stranded DNA polymer brushes by temperature change

To investigate the universality of reversible assembly of cTR-AuNRs in polymer brushes, I attached the cTR-AuNRs-(10:90) in single-stranded (ss) DNA brushes. ssDNA brushes were prepared in Section 3-2-3. I first evaluated the attachment density of cTR-AuNRs in ssDNA brushes from extinction spectra under the incident light perpendicular to the substrate (Figure 3-23a). The quantitative assessment of adsorbed cTR-AuNRs-(10:90) was calculated from the extinction at 400 nm. The cTR-AuNRs-(10:90) adsorption density was quantified as 1500 particles/μm². Correspondingly, the adsorption density was translated into average center-to-center distances between the adsorbed cTR-AuNRs, which were calculated to be approximately 28 nm. Next, the orientation was evaluated by extinction spectrum under the incident light perpendicular to the substrate. cTR-AuNRs-(10:90) immobilized in ssDNA brushes exhibited a distinctly weak L-LSPR intensity, which is significantly lower than that of the T-LSPR indicating a vertical arrangement of cTR-AuNRs-(10:90).

cTR-AuNRs also exhibit temperature responsiveness in ssDNA brushes (Figure 3-23b, c). Moreover, cTR-AuNRs can achieve reversible assembly in the vertical orientation in ssDNA brushes (Figure 3-23d, e). This result is highly consistent with the behavior of cTR-AuNRs in dsDNA brushes.

These results showed that this thermo-responsive assembly/disassembly system is also manifest for polymer brushes composed of ssDNA with a flexible structure, confirming the universality of this system to anionic polymer brushes. Due to the inherent rigidity of dsDNA, I focus on dsDNA for further experimental investigations.

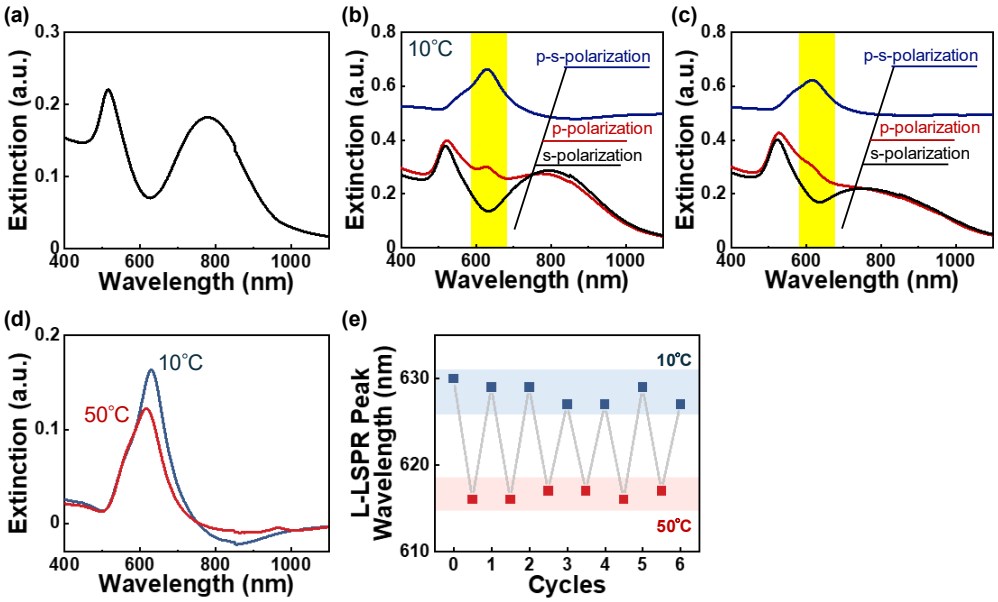


Figure 3-23. (a) Extinction spectrum of cTR-AuNRs-(10:90) in ssDNA brushes at 10°C under incident light perpendicular to the substrate. (b) Extinction spectra of cTR-AuNRs-(10:90) attached in ssDNA brushes under p- (red), s-polarized light (black), and difference extinction spectrum of p- and s-polarized light (blue) at 10°C. (c) Extinction spectra of cTR-AuNRs-(10:90) attached in ssDNA brushes under p- (red), s-polarized light (black), and difference extinction spectrum of p- and s-polarized light (blue) at 50°C. (d) The difference extinction spectrum of cTR-AuNRs-(10:90) under p- and s-polarized light at 10°C (blue) and 50°C (red). (e) cTR-AuNRs-(10:90) L-LSPR peak shift in the difference extinction spectrum in 6 cycles between 10°C (blue) and 50°C (red).

3-3-6. Evaluation of cTR-AuNRs assembly on double-stranded DNA polymer brushes by Finite Difference Time Domain Method

To estimate the numbers of AuNRs in the assembly, we performed an FDTD simulation under the determined AuNR assemblies with various assembly numbers. The p-polarized light tilted at 45 degrees was used to model the assembly of the vertically aligned AuNRs structure. We postulated an AuNR center-to-center distance of 14 nm after assembly (assuming a ligand length of 2 nm and a total ligand span of 4 nm, leaving only ligand-mediated separation between the AuNRs).[101] The initial center-to-center distance between AuNRs as disassembled state was set to be 30 nm based on the experimental results. Given the nanoscale distances between the assemblies in the DNA brushes, the plasmonic coupling between the assemblies cannot be ignored. Therefore, we have used simulations based on periodic structures to analyze (Figure 3-24A). In the experimental results, the wavelength of cTR-AuNRs-(10:90), -(15:85), and -(20:80) immobilized in DNA brushes was blue-shifted from 635 nm to about 615 nm upon heating due to assembly formation (Figure 3-20). Our simulation shows that the separated (disassembled) AuNRs exhibited a peak wavelength of 633 nm, which is close to the experimental result (635 nm). Assemblies of three AuNRs show a peak at 611 nm, corresponding to the experimental results of the peak shift amount (around 25 nm) (Figure 3-24B-i). The comparison of FDTD simulations and experimental results indicate an approximate number of AuNRs in the assembly is regarded to be two to three for cTR-AuNRs-(10:90), -(15:85), and -(20:80) in the DNA brush system. The assembly number of AuNRs freely dispersed in solution was also evaluated by FDTD simulations (Figure 2-13a, b). Solution-dispersed cTR-AuNRs-(10:90) showed blue-shift from 760 nm to about 690 nm upon heating due to assembly formation (Figure 2-11). These shiftings are well-matched to dispersed (single) AuNR (768 nm) and three AuNRs in the assembly (676 nm) in the FDTD

simulation. The FDTD simulations showed a similarity in the number of AuNR in the assemblies formed dispersed in solution and immobilized in DNA brushes, although the peak shift amount is different (Figure 3-24B-ii and Figure 2-13c).

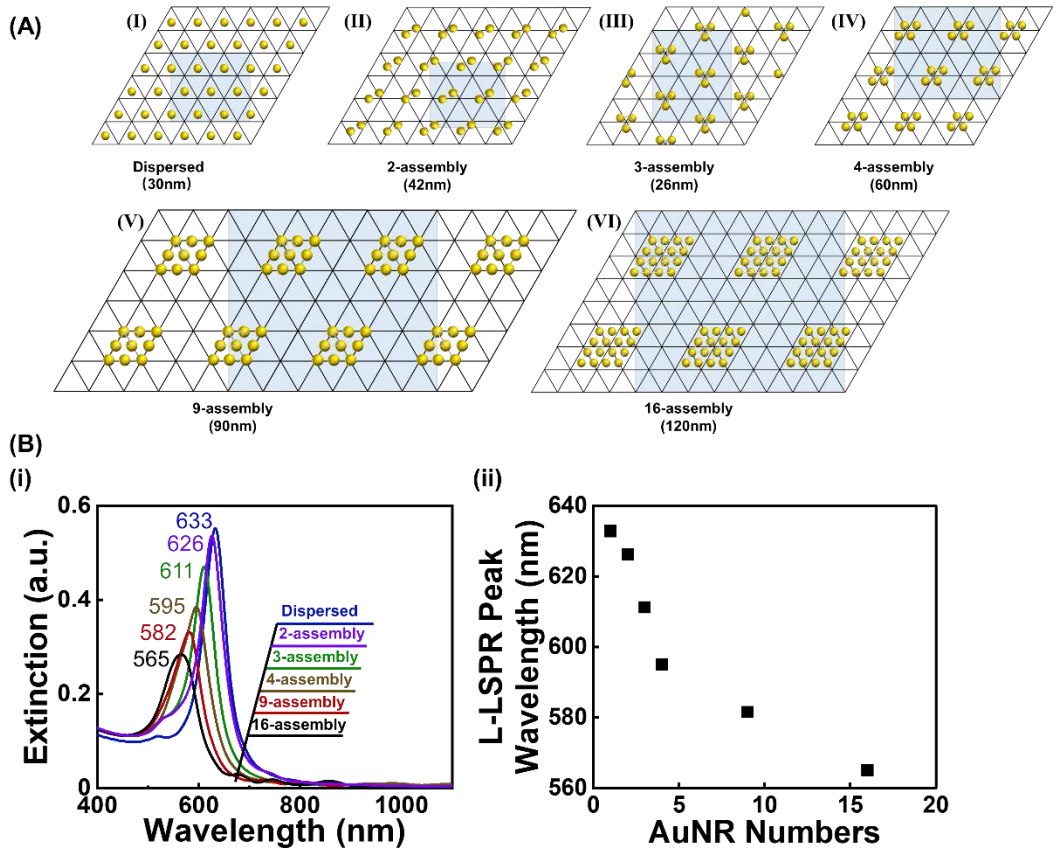


Figure 3-24. (A) Schematic model of the (I) AuNRs immobilized in a DNA brush (AuNRs center-to-center distance is 30 nm); AuNRs assemblies in a DNA brush comprising (II) two, (III) three, (IV) four, (V) nine, and (VI) sixteen nanorods (AuNRs center-to-center distance is 14 nm). The numerical values in parentheses denote the center-to-center distances between the AuNR assemblies**.** (B) (i) Extinction spectra for AuNR assemblies calculated by FDTD simulation under p-polarization at 45 degrees and (ii) their L-LSPR peak wavelength of AuNR assemblies in the arrays with different numbers of AuNRs.

3-3-7. Evaluation of different attachment density of cTR-AuNRs assembly on double-stranded DNA polymer brushes

To investigate the effect of the initial separation distance between AuNRs on their assembly behavior, we immobilized cTR-AuNRs in dsDNA brushes at various densities by varying the concentration of the cTR-AuNRs-(10:90) in solution (Figure 3-25a). The initial center-to-center distances between the AuNRs can be estimated from the AuNR attachment density. All of the cTR-AuNRs-(10:90) showed low L-/T-LSPR, indicating vertical alignments (Figure 3-25b). When AuNRs were immobilized in DNA brushes at a low density of 150 particles/μm^2 (center-to-center distances: 88nm), their initial peak wavelength was observed to be around 720 nm, indicating the presence of plasmon coupling phenomena even in this separation. A progressive blue-shifting was observed depending on increases in the AuNR attachment density (Figure 3-25c).

Then, the effect of initial separation distance on the assembly/disassembly of cTR-AuNRs was investigated by the systematic thermo-responsive experiments with cTR-AuNRs at various initial distances at the separated states at 10°C (Figure 3-26 and Figure 3-27a). The L-LSPR peak of AuNRs gradually undergoes a blue shift as the initial separation distance decreases at 10°C. At the same time, the amount of peak shifting at temperature changes between 10 and 50°C also decreases. This result explains the observed discrepancy in shifting amount for AuNR assemblies dispersed in solution and immobilized in DNA brushes, despite a consistent number of particles in the assemblies. Thus, we conclude this variation results from the different initial distances between AuNRs.

Furthermore, intuitive analyses on the AuNR mobility within polymer brushes were performed by employing a model with greater initial separation distances. For assemblies of AuNRs with a center-to-center distance of 88 nm, they need a movement of

approximately 74 nm based on the assumption of an interstitial gap of 14 nm on assembly (Figure 3-27b). As the averaged DNA chain distance is approximately 8 nm, it is expected that each AuNR is anchored by 2 to 3 DNA strands and wandering from a DNA to another DNA to facilitate assembly. In reality, the AuNRs show remarkable adhesion stability in the DNA brushes without any significant detachment on washing and thermal cycling processes via multi-point anchoring, but perform assembly formation even at largely separated condition, indicating a traveling of considerable distances like a lateral diffusion. During their dynamic repositioning, the AuNRs may dissociate from some DNAs, but the proximity of adjacent DNAs allows their rapid reattachment to neighboring positions. This dynamic relocalization mechanism allows the AuNRs to maintain a stable association with the DNA brush while facilitating flexible spatial adjustments.

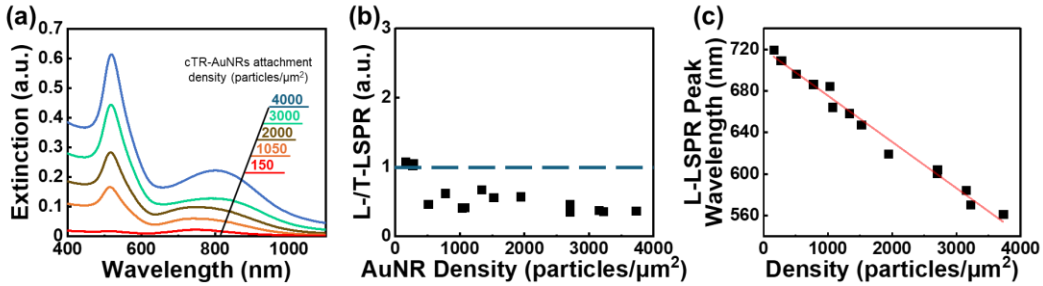


Figure 3-25. (a) Extinction spectra of cTR-AuNRs-(10:90) attached in dsDNA brushes with various attachment density at 10°C under incident light perpendicular to the substrate. (b) L-/T-LSPR values after attaching of cTR-AuNRs-(10:90) against attachment density. The dashed line indicates L-/T-LSPR equal to 1.0. (c) L-LSPR peak wavelength with various cTR-AuNR attachment densities under difference extinction spectrum of p- and s-polarized light.

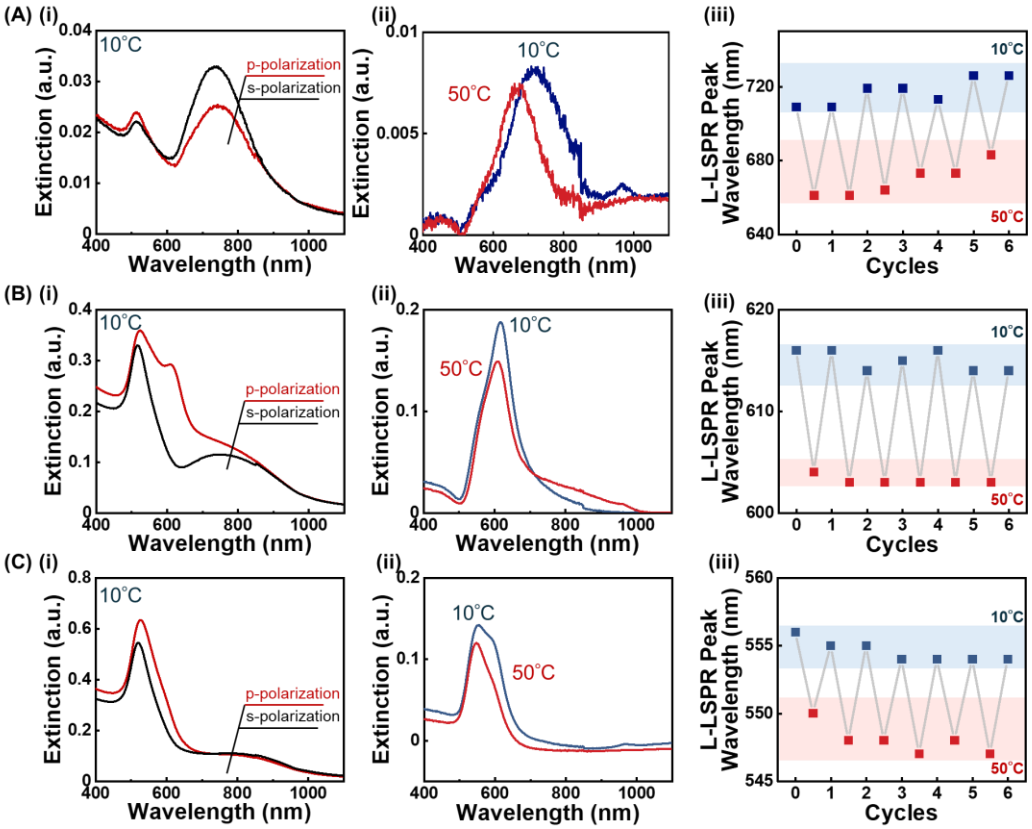


Figure 3-26. The cTR-AuNRs-(10:90) attachment density of (A) 150 particles/μm² (88nm initial distance), (B) 2000 particles/μm² (24nm initial distance), and (C) 3000 particles/μm² (19nm initial distance). (i) Extinction spectra of cTR-AuNRs-(10:90) attached in dsDNA brushes under p- (red) and s-polarized light (black) at 10°C. (ii) The difference extinction spectrum of p- and s-polarized light at 10°C (blue) and 50°C (red). (iii) cTR-AuNRs-(10:90) L-LSPR peak shift in the difference extinction spectrum in 6 cycles between 10°C (blue) and 50°C (red).

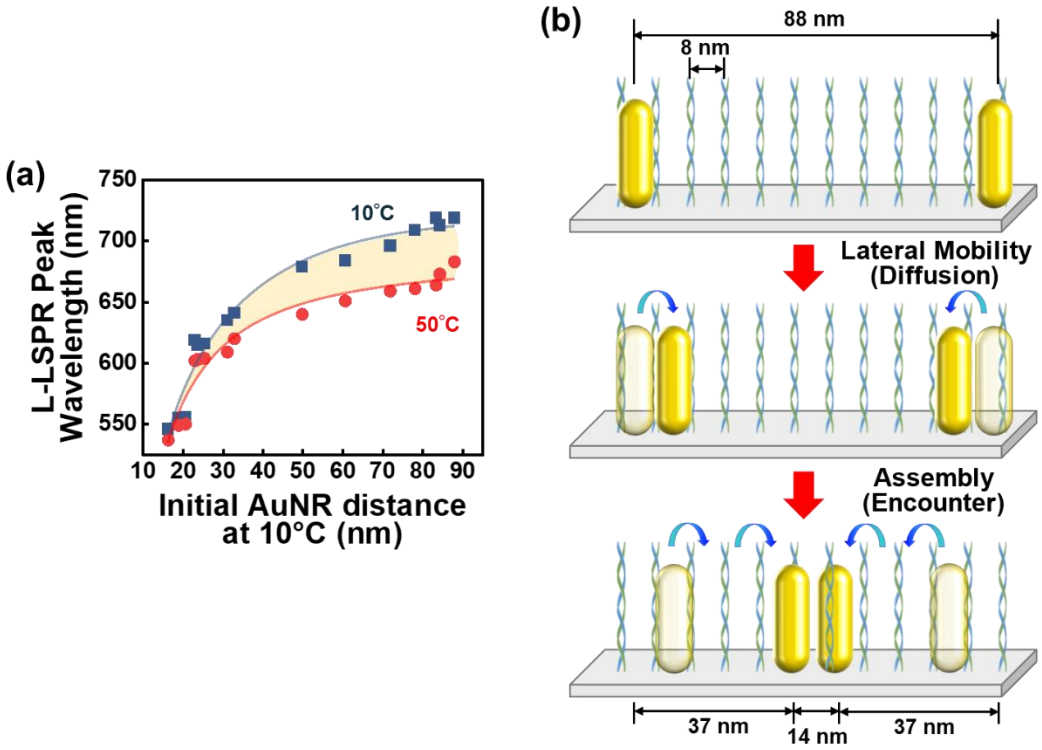


Figure 3-27. (a) L-LSPR peak wavelength (between 10 and 50°C) in differential extinction spectra of cTR-AuNRs-(10:90) with various initial center-to-center distance at disassembled at 10°C. (b) Schematic image of the AuNR assembling process at 150 particles/μm^2 (88 nm initial distance) in DNA brushes.

3-4. Conclusion

In this chapter, I successfully achieved the reversible assembly of cTR-AuNRs with uniform orientation. These results indicate that cTR-AuNRs with moderate charge modification can be attached vertically to DNA brushes, demonstrating precise control over their orientation. I observed that the number of assembled cTR-AuNRs both dispersed in solution and attached to DNA brushes is nearly identical. Notably, the assembly rate of cTR-AuNRs attached to DNA brushes is significantly faster than those dispersed in solution, suggesting that this system enhances the assembly efficiency of AuNRs. Furthermore, by changing the density of cTR-AuNRs within the DNA brushes, I found that the amount of displacement is related to their initial positions. By increasing the distance between AuNRs, I understand that cTR-AuNRs have good mobility in the DNA brushes. This model provides a comprehensive understanding of the dynamic behavior of cTR-AuNRs in the DNA brush system, highlighting their potential for applications requiring precise and efficient nanomaterial assembly. These conclusions underscore the effectiveness of using DNA brushes for the controlled assembly of AuNRs, offering significant advances in the development of nanomaterial systems with uniform orientation and improved assembly efficiency. This research provides a solid foundation for future studies aimed at optimizing the functional properties of thermo-responsive nanomaterials for various applications, including biosensing, photonics, and nanodevices.

Chapter 4

General Conclusion

In this thesis, I focused on the reversible assembly control of gold nanorods in polymer brushes with uniform orientation for their plasmonic control. In this chapter, I summarize this thesis and afford the significance and prospects.

In chapter 2, I have successfully prepared the thermo-responsive cTR-AuNRs with different cationic charges. These cTR-AuNRs exhibit significant temperature response in the range of 10 to 50ºC when dispersed in solution. The observed hysteresis during the heating and cooling processes can be attributed to the rapid dispersion kinetics of the AuNRs. Furthermore, the addition of cationic ligands effectively increases the response temperature of the AuNRs and decreases the number of AuNRs involved in the assemblies.

In chapter 3, I successfully achieved the reversible assembly of cTR-AuNRs with uniform orientation. These results indicate that cTR-AuNRs with moderate charge modification can be attached vertically to DNA brushes, demonstrating precise control over their orientation. I observed that the number of assembled cTR-AuNRs both dispersed in solution and attached to DNA brushes is nearly identical. Notably, the assembly rate of cTR-AuNRs attached to DNA brushes is significantly faster than those dispersed in solution, suggesting that this system enhances the assembly efficiency of AuNRs. Furthermore, by changing the density of cTR-AuNRs within the DNA brushes, I found that the amount of displacement is related to their initial positions. By increasing the distance between AuNRs, I understand that cTR-AuNRs have good mobility in the DNA brushes. This model provides a comprehensive understanding of the dynamic behavior of cTR-AuNRs in the DNA brush system, highlighting their potential for applications requiring precise and efficient nanomaterial assembly. These conclusions underscore the effectiveness of using DNA brushes for the controlled assembly of AuNRs, offering significant advances in the development of nanomaterial systems with uniform

orientation and improved assembly efficiency. This research provides a solid foundation for future studies aimed at optimizing the functional properties of thermo-responsive nanomaterials for various applications, including biosensing, photonics, and nanodevices.

In this thesis, I developed a temperature-responsive plasmon switching system with vertically aligned cTR-AuNRs in DNA brushes by utilizing moderate electrostatic interactions. The assembly/disassembly of cTR-AuNRs in the DNA brushes was realized while maintaining uniform (vertical) orientation through temperature-induced changes in surface properties (hydrophilicity/hydrophobicity). This assembly/disassembly process was reversible. Furthermore, AuNRs immobilized in the DNA brushes showed significantly improved assembly/disassembly kinetics compared to those dispersed in solution. FDTD simulations indicated the number of AuNRs within the assemblies was three in the DNA brushes as well as when dispersed in solution. By modulating the immobilization density of AuNRs in the DNA brushes, the mobility of AuNRs in the DNA brushes was qualitatively elucidated, indicating their traveling ability for considerable distances via a lateral diffusion. This platform offers great potential for the design of hybrid materials composed of anisotropic nanoparticles and polymer brushes.

References

1 M. Torres, C. A. Rosselló, P. Fernández-García, V. Lladó, O. Kakhlon, P. V. Escribá, *Int. J. Mol. Sci.* **2020**, *21(7),* 2322.

2 A. Naito, I. Kawamura, *Membranes* **2022**, *12(7)*, 672.

3 L. M. P. Chataigner, N. Leloup, B. J. C. Janssen, *Front Mol Biosci.* **2020**, *7*, 129.

4 M. Lal, M. Caplan, *PHYSIOLOGY* **2011**, *26*, 34-44.

5 K. Imamura, H. Yoshida, M. Ozaki, *Soft Matter* **2016**, *12*, 750.

6 T. Jin, B. Zalar, A. Lebar, M. Vilfan, S. Zumer, D. Finotello, *The European Physical Journal E* **2005**, *16*, 159.

7 H. W. Chen, J. H. Lee, B. Y. Lin, S. Chen, S. T. Wu, *Light: Science & Application* **2018**, *7*, 17168.

8 P. Zhang, L. T. de Haan, M. G. Debije, A. P. H. J. Schenning, *Light: Science & Applications* **2022**, *11*, 248.

9 M. Clark, *Physics World* **1991**, *4*, 21.

10 F. Li, S. Zhang, X. Wang, Y. Xu, S. Chung, *SID Symposium Digest of Technical Papers* **2022**, *53*, 944.

11 S. I. Stupp, R. H. Zha, L. C. Palmer, H. Cui, R. Bitton, *Faraday Discuss* **2013**, *166*, 9-30.

12 Y.-C. Lee, J.-Y. Moon, in *Introduction to Bionanotechnology*, ed. by Young-Chul Lee, Ju-Young Moon, Springer Singapore, Singapore, **2020**, pp. 79–92.

13 D. Badgurjar, M. Huynh, B. Masters, A. Wuttig, *J Am Chem Soc* **2023**, *145*, 17734.

14 X. Z. Wang, Y. Q. Chen, X. Z. Chen, X. K. Jiang, Z.-T. Li, *Progress in Chemistry* **2005**, *17*, 451.

15 H. Zhao, S. Zhang, S. Li, X. Song, W. Liu, B. Liu, M. Dong, *RSC Adv* **2015**, *5*, 103316.

16 C. Solís-Calero, J. Ortega-Castro, J. Frau, F. Munõz, *Oxid Med Cell Longev* **2015**, 319505.

17 X. Shi, X. Li, M. Kohram, A. W. Smith, *Biophys J* **2016**, *110*, 573a.

18 N. Nagradova, *Current Protein & Peptide Science* **2007***, 8,* 273-282.

19 R. Seckler, R. Jaenicke, *The FASEB Journal* **1992**, *6*, 2545.

20 E. Braselmann, P. L. Clark, *J Phys Chem Lett* **2012**, *3*, 1063-1071.

21 Alberts B, Johnson A, Lewis J, in *Molecular Biology of the Cell. 4th edition.; 2002.*, Garland Science, New York, **2002**, Chap. 16.

22 S. Yadav, A. K. Sharma, P. Kumar, *Front. Bioeng. Biotechnol* **2020**, *8*, 127.

23 H. Karballaei Mirzahosseini, M. Sheikhi, F. Najmeddin, M. Shirangi, M. Mojtahedzadeh, *Drug Metab Rev* **2023**, *55*, 140.

24 J. Yang, H. An, H. Wang, *ACS Appl Bio Mater* **2021**, *4*, 24.

25 H. Sun, X. Li, Q. Liu, H. Sheng, L. Zhu, *J Drug Target* **2024**, 1-35.

26 Z. Zhao, F. Liang, S. Liu, *Curr Top Med Chem* **2017***, 17,* 1829-1842.

27 A. Belluati, S. Jimaja, R. J. Chadwick, C. Glynn, M. Chami, D. Happel, C. Guo, H. Kolmar, N. Bruns, *Nat Chem* **2024**, *16*, 564.

28 A. Majerle, D. T. Schmieden, R. Jerala, A. S. Meyer, *Biochemistry* **2019**, *58*, 2095.

29 S. Agarwal, M. A. Klocke, P. E. Pungchai, E. Franco, *Nat Commun* **2021**, *12*, 3557.

30 R. Rubio-Sánchez, G. Fabrini, P. Cicuta, L. Di Michele, *Chemical Communications* **2021**, *57*, 12725.

31 M. A. R. Khan, M. S. Al Mamun, M. A. Habib, A. B. M. N. Islam, M. Mahiuddin, K. M. R. Karim, J. Naime, P. Saha, S. K. Dey, M. H. Ara, *Results in Chemistry* **2022**, *4*, 100478.

32 H. Hei, R. Wang, X. Liu, L. He, G. Zhang, *Soft Nanoscience Letters* **2012**, *02*, 34.

33 M. Rawat, J. Singh, H. Kaur, *J Nanomed Res* **2018**, *7*, 228-229.

34 D. Varade, K. Haraguchi, *Soft Matter* **2012**, *8*, 3743.

35 A. Turak, *Photonics North (PN) Journal* **2023**, *00*, 58661.

36 M. Sanz-Paz, C. Ernandes, J. U. Esparza, G. W. Burr, N. F. van Hulst, A. Maitre, L. Aigouy, N. Bonod, T. Gacoin, M. F. Garcia-Parajo, S. Bidault, M. Mivelle, 2019 Conference on Lasers and Electro-Optics Europe & European Quantum Electronics Conference (CLEO/Europe-EQEC), 1.

37 C.-N. Shauo, C.-G. Chao, T. M. Wu, H.-J. Shy, *Mater Trans* **2007**, *48*, 1143.

38 K. A. Willets, R. P. Van Duyne, *Annu Rev Phys Chem* **2007**, *58*, 267.

39 K.-C. Lee, S.-J. Lin, C.-H. Lin, C.-S. Tsai, Y.-J. Lu, *Surf Coat Technol* **2008**, *202*, 5339.

40 T. Sandu, *Journal of Nanoparticle Research* **2012**, *14*, 905.

41 C. Noguez, *The Journal of Physical Chemistry C* **2007**, *111*, 3806.

42 T. D. Phuc, M. Yoshino, A. Yamanaka, T. Yamamoto, *International Journal of Automation Technology* **2014**, *8*, 74.

43 L. C. Ugwuoke, T. Mančal, T. P. J. Krüger, *Plasmonics* **2020**, *15*, 189.

44 *Controlled Nanofabrication*, ed. by Liu Ru Shi, Jenny Stanford Publishing, **2012**.

45 I. Ielo, G. Rando, F. Giacobello, S. Sfameni, A. Castellano, M. Galletta, D. Drommi, G. Rosace, M. R. Plutino, *Molecules* **2021***, 26,* 5823.

46 R. Adnan Al-wardy, S. Khalid Rahi, *Samarra J. Pure Appl. Sci.* **2021**, *3*, 74-86.

47 J. Zhang, L. Mou, X. Jiang, *Chem Sci* **2020**, *11*, 923.

48 M.-C. Daniel, D. Astruc, *Chem Rev* **2004**, *104*, 293.

49 J. Cai, A. Watanabe, in *New Polymeric Materials Based on Element-Blocks*, ed. by Yoshiki Chujo, Springer Singapore, Singapore, **2019**, pp. 385–412.

50 J. Zhang, L. Mou, X. Jiang, *Chem Sci* **2020**, *11*, 923.

51 Y. Wang, K. Sentosun, A. Li, M. Coronado-Puchau, A. Sánchez-Iglesias, S. Li, X. Su, S. Bals, L. M. Liz-Marzán, *Chemistry of Materials* **2015**, *27*, 8032.

52 W. Qian, M. Murakami, Y. Ichikawa, Y. Che, Proc.SPIE, 82320P.

53 W. Xiang, Z. Zhu, X. Song, C. Zhong, C. Wang, Y. Ma, *RSC Adv* **2016**, *6*, 102057.

54 L. Ye, B. Qi, T. Pearson, Y. Cordeau, O. T. Mefford, T. M. Crawford, *J Appl Phys* **2014**, *115*, 17B513.

55 B. A. Parviz, D. Ryan, G. M. Whitesides, *IEEE Transactions on Advanced Packaging* **2003**, *26*, 233.

56 F. S. Ou, M. Hu, I. Naumov, A. Kim, W. Wu, A. M. Bratkovsky, X. Li, R. S. Williams, Z. Li, *Nano Lett* **2011**, *11*, 2538.

57 H. Kohno, S. Takeda, *Appl Phys Lett* **2003**, *83*, 1202.

58 A. F. Versiani, L. M. Andrade, E. M. N. Martins, S. Scalzo, J. M. Geraldo, C. R. Chaves, D. C. Ferreira, M. Ladeira, S. Guatimosim, L. O. Ladeira, F. G. da Fonseca, *Future Virol* **2016**, *11*, 293.

59 A. Hua, *Highlights in Science, Engineering and Technology*, **2022**, *26*, 252-258.

60 R. A. Sperling, P. Rivera Gil, F. Zhang, M. Zanella, W. J. Parak, *Chem Soc Rev* **2008**, *37*, 1896.

61 J. Zhang, L. Mou, X. Jiang, *Chem Sci* **2020**, *11*, 923.

62 J. ZHAO, B. BO, Y.-M. YIN, G.-X. LI, *Nano Life* **2012**, *02*, 1230008.

63 G. Han, P. Ghosh, V. M. Rotello, *Nanomedicine* **2007**, *2*, 113.

64 Q. Yang, J. Seo, W.-J. Kim, S. Jung, B. Tabibi, J. Vazquez, J. Austin, D. Temple, *SPIE*, **2009**, *1*, 727617.

65 W. R. Glomm, *J Dispers Sci Technol* **2005**, *26*, 389.

66 D. Decarolis, Y. Odarchenko, J. J. Herbert, C. Qiu, A. Longo, A. M. Beale, *Physical Chemistry Chemical Physics* **2020**, *22*, 18824.

67 K. Wongyai, P. Wintachai, R. Maungchang, P. Rattanakit, *J Nanomater* **2020**, 1320274.

68 F. Mancin, L. J. Prins, F. Rastrelli, P. Scrimin, in *Supramolecular Chemistry in Water*, **2019**, 413–447.

69 A. Waheed, N. Ghazal, *Journal of Drug Delivery and Therapeutics* **2020**, *10*, 151.

70 B. Shelembe, N. T. Mahlangeni, R. Moodley, *Advances in Natural Sciences: Nanoscience and Nanotechnology* **2019**, *10*, 045002.

71 R. K. M. Raguindin, C. C. Mercado, *RSC Adv* **2023**, *13*, 24211.

72 K. Ge, Y. Hu, G. Li, *Biosensors* **2022**, *12*, 941.

73 A. Scroccarello, F.D. Pelle, M. D. Carlo, D. Compagnone, *Anal Chim Acta* **2023**, 340594.

74 D. J. Lee, D. Y. Kim, *Sci Rep* **2021**, *11*, 22399.

75 T. Liu, T. Keiper, X. Wang, G. Yang, D. Hallinan, J. Zhao, P. Xiong, *ACS Appl Mater Interfaces* **2017**, *9*, 43363.

76 D. Tonelli, E. Scavetta, I. Gualandi, *Sensors* **2019**, *19*, 1186.

77 R. Peng, T. Zhang, S. Yan, Y. Song, X. Liu, J. Wang, *Nanomaterials* **2023**, *13*, 2968.

78 Z. Huang, *Molecules* **2023***, 28*, 8104.

79 H.-N. Barad, H. Kwon, M. Alarcón-Correa, P. Fischer, *ACS Nano* **2021**, *15*, 5861.

80 P. Si, N. Razmi, O. Nur, S. Solanki, C. M. Pandey, R. K. Gupta, B. D. Malhotra, M. Willander, A. de la Zerda, *Nanoscale Adv* **2021**, *3*, 2679.

81 Y. Zheng, C. H. Lalander, T. Thai, S. Dhuey, S. Cabrini, U. Bach, *Angewandte Chemie International Edition* **2011**, *50*, 4398.

82 T. Bartschmid, A. Farhadi, M. E. Musso, E. S. A. Goerlitzer, N. Vogel, G. R. Bourret, *ACS Appl Nano Mater* **2022**, *5*, 11839.

83 A. Mourkas, A. Zarlaha, N. Kourkoumelis, I. Panagiotopoulos, *Nanomaterials* **2021**, *11*, 1030.

84 M. Wang, C. Gao, L. He, Q. Lu, J. Zhang, C. Tang, S. Zorba, Y. Yin, *J Am Chem Soc* **2013**, *135*, 15302.

85 E. Kopperger, J. List, S. Madhira, F. Rothfischer, D. C. Lamb, F. C. Simmel, *Science* **2018**, *359*, 296-301.

86 M. Sastry, A. Kumar, S. Datar, C. V Dharmadhikari, K. N. Ganesh, *Appl Phys Lett* **2001**, *78*, 2943.

87 M.-L. Lin, F. Yang, J. S. Peng, S. Lee, *J Appl Phys* **2014**, *115*, 054312.

88 W. Liu, C. Wang, H. Ding, J. Shao, Y. Ding, *Appl Surf Sci* **2016**, *370*, 184.

89 N. Chandrasekharan, P. V Kamat, *Nano Lett* **2001**, *1*, 67.

90 Y. Sekizawa, H. Mitomo, M. Nihei, S. Nakamura, Y. Yonamine, A. Kuzuya, T. Wada, K. Ijiro, *Nanoscale Adv* **2020**, *2*, 3798.

91 Y. C. Kim, R. J. Composto, K. I. Winey, *ACS Nano* **2023**, *17*, 9224.

92 D. Yao, H. Li, Y. Guo, X. Zhou, S. Xiao, H. Liang, *Chemical Communications* **2016**, *52*, 7556.

93 J. A. Tullman, W. F. Finney, Y.-J. Lin, S. W. Bishnoi, *Plasmonics* **2007**, *2*, 119.

94 W. Li, I. Kanyo, C.-H. Kuo, S. Thanneeru, J. He, *Nanoscale* **2015**, *7*, 956.

95 T. Ding, V. K. Valev, A. R. Salmon, C. J. Forman, S. K. Smoukov, O. A. Scherman, D. Frenkel, J. J. Baumberg, *PNAS* **2016**, *113*, 5503.

96 J. Dietler, C. Liang, S. Frank, A.-K. Müller, A. Greiner, A. Möglich, *Adv Biol* **2021**, *5*, 2000179.

97 K. Saito, K. McGehee, Y. Norikane, *Particle & Particle Systems Characterization* **2022**, *39*, 2200123.

98 A. Abbas, R. Kattumenu, L. Tian, S. Singamaneni, *Langmuir* **2013**, *29*, 56.

99 R. Iida, H. Mitomo, K. Niikura, Y. Matsuo, K. Ijiro, *Small* **2018**, *14, 1704230*.

100 R. Iida, H. Mitomo, Y. Matsuo, K. Niikura, K. Ijiro, *Journal of Physical Chemistry C* **2016**, *120*, 15846.

101 K. Xiong, H. Mitomo, X. Su, Y. Shi, Y. Yonamine, S. Sato, K. Ijiro, *Nanoscale Adv* **2021**, *3*, 3762.

102 J. Chidiebere Mba, H. Mitomo, Y. Yonamine, G. Wang, Y. Matsuo, K. Ijiro, *Nanomaterials* **2022**, *12*, 1421.

103 G. Wang, L. Yu, Y. Akiyama, T. Takarada, M. Maeda, *Biotechnol J* **2018**, *13,* 1800090.

104 J. Kruse, A. Rao, A. Sánchez-Iglesias, J. L. Montaño-Priede, A. Iturrospe Ibarra, E. Lopez, A. Seifert, A. Arbe, M. Grzelczak, *Chemistry - A European Journal* **2024**, *30,* e202302793.

105 H. Mitomo, K. Niikura, K. Ijiro, in *Stimuli-Responsive Interfaces: Fabrication and Application*, ed. by Takeshi Kawai, Mineo Hashizume, Springer Singapore, Singapore, **2017**, pp. 127–145.

106 G. Zhang, J. B. Jasinski, J. L. Howell, D. Patel, D. P. Stephens, A. M. Gobin, *Nanoscale Res Lett* **2012**, *7*, 337.

107 R. J. Hickey, M. Seo, Q. Luo, S.-J. Park, *Langmuir* **2015**, *31*, 4299.

108 Y. Wang, A. Dang, Z. Zhang, R. Yin, Y. Gao, L. Feng, S. Yang, *Advanced Materials* **2020**, *32*, 2004270.

109 T. Kudo, S.-J. Yang, H. Masuhara, *Nano Lett* **2018**, *18*, 5846.

110 F. Ren, C. Yesildag, Z. Zhang, M. C. Lensen, *Polymers* **2017**, *9*, 154.

111 H. P. Lee, K. A. Deo, J. Jeong, M. Namkoong, K. Y. Kuan, L. Tian, A. K. Gaharwar, *Adv Mater Interfaces* **2022**, *9*, 2201186.

112 P. Wang, J. Sun, Z. Lou, F. Fan, K. Hu, Y. Sun, N. Gu, *Advanced Materials* **2016**, *28*, 10801.

113 R. J. Hickey, M. Seo, Q. Luo, S.-J. Park, *Langmuir* **2015**, *31*, 4299.

114 B. Miranda, R. Moretta, S. De Martino, P. Dardano, I. Rea, C. Forestiere, L. De Stefano, *J Appl Phys* **2021**, *129*, 033101.

115 J. G. Turner, J. H. Og, C. J. Murphy, *Soft Matter* **2020**, *16*, 6582.

116 S. Lin, S. Jiang, Y. Zhang, Z. Dai, Y. Dai, F. Xia, X. Zhang, *Gold Bull* **2021**, *54*, 59.

117 M. A. De Jesús-Téllez, I. Felix-Serrano, R. J. Rodríguez-González, D. Navarro-Rodríguez, L. Larios-López, *Polymer* **2020**, *205*, 122837.

118 S. D. García Schejtman, P. A. Mercadal, M. L. Picchio, A. V Veglia, E. A. Coronado, *The Journal of Physical Chemistry C* **2022**, *126*, 9979.

119 C. Wang, Y. Li, X. Liu, J. Fu, J. Shen, W. Qi, *J Mol Liq* **2023**, *380*, 121718.

120 H. Mitomo, K. Horie, Y. Matsuo, K. Niikura, T. Tani, M. Naya, K. Ijiro, *Adv Opt Mater* **2016**, *4*, 259.

121 S. Nakamura, H. Mitomo, Y. Yonamine, K. Ijiro, *Chem Lett* **2020**, *49*, 749.

122 Y. C. Kim, R. J. Composto, K. I. Winey, *ACS Nano* **2023**, *17*, 9224.

123 D. Boyaciyan, **2019**, Functional Coatings with Colorimetric Properties: the Influence of Electrostatic Interaction and Hydrogen Bonding on the Assembly of Gold Nanoparticles in Polymer Brushes, *Universitäts- und Landesbibliothek Darmstadt*.

124 K. Hendrich, W. Peng, P. Vana, *Polymers* **2020**, *12*, 1214.

125 C. Zhou, T. Sun, M. Gong, Z. Xu, L. Zhang, Q. Li, M. Du, X. Kang, Y. Liu, *Mater Chem Front* **2021**, *5*, 7323.

126 A. Eskandari Nasrabad, R. Laghaei, R. D. Coalson, *Int J Mol Sci* **2023**, *24*, 832.

127 S. Christau, T. Moeller, J. Genzer, R. Koehler, R. von Klitzing, *Macromolecules* **2017**, *50*, 7333.

128 Y. Du, J. Jin, H. Liang, W. Jiang, *Langmuir* **2019**, *35*, 8316.

129 C. E. Neri-Cruz, F. M. E. Teixeira, J. E. Gautrot, *Chemical Communications* **2023**, *59*, 7534.

130 A. Degirmenci, G. Yeter Bas, R. Sanyal, A. Sanyal, *Bioconjug Chem* **2022**, *33*, 1672.

131 L. Yin, L. Liu, N. Zhang, *Chemical Communications* **2021**, *57*, 10484.

132 S. Lamping, C. Buten, B. J. Ravoo, *Acc Chem Res* **2019**, *52*, 1336.

133 N. Li, P. Zhao, D. Astruc, *Angewandte Chemie International Edition* **2014**, *53*, 1756.

134 J. Cao, T. Sun, K. T. V. Grattan, *Sensors and Actuators B: Chemical* **2014**, *195*, 332-351.

135 M. L. Taylor, R. E. Wilson, K. D. Amrhein, X. Huang, *Bioengineering* **2022**, *9*, 200.

136 C. Liu, P. Gong, Y. Liang, Z. Wang, L. Wang, *Medziagotyra* **2019**, *26*, 243.

137 L. Fu, Y. Liu, W. Wang, M. Wang, Y. Bai, E. L. Chronister, L. Zhen, Y. Yin, *Nanoscale* **2015**, *7*, 14483.

138 H. Chen, L. Shao, Q. Li, J. Wang, *Chem Soc Rev* **2013**, *42*, 2679.

139 Y. Wang, L. Tang, *Biosens Bioelectron* **2015**, *67*, 18.

140 Y. Huang, X. Zhang, E. Ringe, M. Hou, L. Ma, Z. Zhang, *Sci Rep* **2016**, *6*.

141 Y. Rong, L. Song, P. Si, L. Zhang, X. Lu, J. Zhang, Z. Nie, Y. Huang, T. Chen, *Langmuir* **2017**, *33*, 13867.

142 N. Albarghouthi, P. MacMillan, C. L. Brosseau, *Analyst* **2021**, *146*, 2037.

143 H. Zhang, Y. Liu, M. F. S. Shahidan, C. Kinnear, F. Maasoumi, J. Cadusch, E. M. Akinoglu, T. D. James, A. Widmer-Cooper, A. Roberts, P. Mulvaney, *Advanced Optical Materials* **2022**, *10*, 2200179.

144 T. Du, J. Schneider, A. K. Srivastava, A. S. Susha, V. G. Chigrinov, H. S. Kwok, A. L. Rogach, *ACS Nano* **2015**, *9*, 11049.

145 K. R. Ryu, J. W. Ha, *Analyst* **2021**, *146*, 3543.

146 H. Fu, N. Ding, D. Ma, Q. Xu, B. Lin, B. Qiu, Z. Lin, L. Guo, *Biosensors* **2023**, *13*.

147 C.-H. Yeh, Z.-Y. Liang, Y.-C. Lin, C.-H. Ma, Y.-H. Chu, K. Suenaga, P.-W. Chiu, *ACS Appl Electron Mater* **2020**, *2*, 3898.

148 A. Yu. Pavlov, K. N. Tomosh, V. Yu. Pavlov, D. N. Slapovskiy, A. V Klekovkin, I. A. Ivchenko, *Nanobiotechnology Reports* **2022**, *17*, S45.

149 H. Wu, Q. Huang, Y. Shi, J. Chang, S. Lu, *Nano Res* **2023**, *16*, 9142.

150 W. Liu, D. Cao, D. Cheng, *Energy Technology* **2021**, *9*, 2000855.

151 S. Anantharaj, S. Noda, *Small* **2020**, *16*, 1905779.

152 S. Nakamura, H. Mitomo, M. Aizawa, T. Tani, Y. Matsuo, K. Niikura, A. Pike, M. Naya, A. Shishido, K. Ijiro, *ACS Omega* **2017**, *2*, 2208.

153 S. Nakamura, H. Mitomo, Y. Sekizawa, T. Higuchi, Y. Matsuo, H. Jinnai, K. Ijiro, *Langmuir* **2020**, *36*, 3590.

154 T. K. Sau, C. J. Murphy, *Langmuir* **2004**, *20*, 6414.

155 P. B. Johnson, R. W. Christy, *Phys Rev B* **1972**, *6*, 4370.

156 A. Brioude, X. C. Jiang, M. P. Pileni, *J Phys Chem B* **2005**, *109*, 13138.

157 Y. Hong, Y. M. Huh, D. S. Yoon, J. Yang, *Journal of Nanomaterials*, **2012**, 759830.

158 S. Chakraborty, S. W. Bishnoi, V. H. Pérez-Luna, *The Journal of Physical Chemistry C* **2010**, *114*, 5947.

159 C. H. Ni, X. X. Zhu, Q. L. Wang, X. Y. Zeng, *Chinese Chemical Letters* **2007**, *18*, 79.

160 N. Gryson, *Anal Bioanal Chem* **2010**, *396*, 2003.

161 Y. Sekizawa, Y. Hasegawa, H. Mitomo, C. Toyokawa, Y. Yonamine, K. Ijiro, *Adv Mater Interfaces* **2024**, *11*, 2301066.

List of academic presentation

1. The 21st RIES-Hokudai International Symposium (December 10th - 11st, 2020)

   “Effect of temperature on the orientation of gold nanorods aligned on the DNA brush” (Poster, December 10th)

   ○Jingyan YANG, Hideyuki MITOMO, Yu SEKIZAWA, Yusuke YONAMINE, Kuniharu IJIRO

2. 第 70 回高分子年次大会 (May 26th - 28th, 2021)

   “Reversible assembly of temperature responsive gold nanorods immobilized in a DNA brush substrate” (Poster, May 26th)

   ○Jingyan YANG, Hideyuki MITOMO, Yu SEKIZAWA, Yusuke YONAMINE, Kuniharu IJIRO

3. 第 31 回バイオ・高分子シンポジウム (June 24th - 25th, 2021)

   “Thermo-responsive assembly of nanoparticle in DNA brushes” (Poster, June 24th)

   ○Jingyan YANG, Hideyuki MITOMO, Yu SEKIZAWA, Yusuke YONAMINE, Kuniharu IJIRO

4. 生体機能関連化学部会若手の会 第 32 回サマースクール (July 15th - 16th , 2021)

   “Thermo-responsive assembly control of gold nanoparticles in DNA brushes” (Poster, July 16th)

   ○Jingyan YANG, Hideyuki MITOMO, Yu SEKIZAWA, Yusuke YONAMINE, Kuniharu IJIRO

5. 2021 年度北海道高分子若手研究会 (August 21st, 2021)

   “Temperature-responsive GNRs assembly/disassembly control in DNA brushes” (Poster, August 21st)

   ○Jingyan YANG, Hideyuki MITOMO, Yu SEKIZAWA, Yusuke YONAMINE, Kuniharu IJIRO

6. 第 7 回部局横断シンポジウム (October 1st, 2021)

   “Gold nanorods reversible assembly control in a DNA brush substrate by temperature” (Poster, October 1st)

   ○Jingyan YANG, Hideyuki MITOMO, Yu SEKIZAWA, Yusuke YONAMINE, and Kuniharu IJIRO

7. Pacifichem 2021 (December 16th - 18th, 2021)

   “Reversible assembly of gold nanorods in response to temperature in a DNA brush” (Poster, December 20th)

   ○Jingyan YANG, Hideyuki MITOMO, Yu SEKIZAWA, Yusuke YONAMINE, and Kuniharu IJIRO

8. 第 56 回高分子学会北海道支部研究発表会 (January 24th, 2022)

   “Temperature-responsive GNR: reversible assembly control using DNA brushes” (Oral, January 24th)

   ○Jingyan YANG, Hideyuki MITOMO, Yu SEKIZAWA, Yusuke YONAMINE, and Kuniharu IJIRO

9. THE 22ND INTERNATIONAL VACUUM CONGRESS IVC-22（September 11st - 16th, 2022）

   “Flexible control of the GNR assembly disassembly in DNA brushes as a 2D layer” (Oral, September 15th)

   ○Jingyan YANG, Hideyuki MITOMO, Yu SEKIZAWA, Yusuke YONAMINE, and Kuniharu IJIRO

10. The 73rd Divisional Meeting of Division of Colloid and Surface Chemistry (September 20th - 22nd, 2022)

    “Reversible assembly of gold nanorods in a DNA brush substrate in response to temperature” (Oral, September 20th)

    ○Jingyan YANG, Hideyuki MITOMO, Yu SEKIZAWA, Yusuke YONAMINE, and Kuniharu IJIRO

11. 日本化学会第 103 回春季年会 (2023) (March 22nd - 25th) (Award)

    “Thermo-responsive Gold nanorods reversibly assemble flexible control with uniform orientation using DNA brushes” (Oral, March 23th)

    ○Jingyan YANG, Hideyuki MITOMO, Yu SEKIZAWA, Yusuke YONAMINE, and Kuniharu IJIRO

12. 第 37 回高分子学会年次大会 (June 5th - 7th)

    “Control of Temperature-Responsive Gold Nanorod Assembly with Uniform Orientation on dsDNA Brush Substrate” (Oral, June 6th)

    ○Jingyan YANG, Hideyuki MITOMO, Yu SEKIZAWA, Yusuke YONAMINE, and Kuniharu IJIRO

Acknowledgement

As I reach the culmination of my doctoral journey, I find myself reflecting on the incredible support and guidance I have received during these transformative three years. This dissertation would not have been possible without the contributions of many individuals to whom I am deeply grateful.

First and foremost, I would like to express my deepest gratitude to Prof. Kuniharu IJIRO and Associate Prof. Hideyuki MITOMO. Their guidance has been invaluable in shaping this research. I am also extremely grateful for your insightful discussions and constructive criticism. Your expertise and attention to detail have greatly enriched my work. Your willingness to provide feedback and your commitment to my progress is greatly appreciated. I have learned so much under your mentorship and am deeply grateful for the opportunities you have provided.

My sincere thanks also go to Associate Prof. Xu SHI (Research Institute for Electronic Science, Hokkaido University) for his guidance and support with FDTD simulations and for being readily available to address any questions or problems that arose.

I would like to extend my heartfelt thanks to the teaching assistants and lab technicians who supported me throughout this journey. To Assistant Prof. Yusuke YONAMINE, thank you for your assistance, which has greatly enriched my knowledge.

I am also grateful to Postdoc Takehiro YACHI, Ms. Chie TAKEUCHI, Ms. Aki OKUHARA, Dr. MBA Joshua CHIDIEBERE, Dr. Kun XIONG, Dr. Yu Sekizawa, Dr. Han LIN, Ms. Melda TASPIKA, Ms. Yali SHI, Mr. Ryo SUGIYAMA, Ms. Wenting WEI, Ms. Zhiyu HE, Mr. Yingqi MU, Mr. Tianxu GAO, Mr. Dongyu ZHANG, Mr. Haoran ZHANG, Mr. Abdul KAIYUM, Mr. Weijie CHEAH, Mr. Kaito SHISHIDO, Ms. Yuka HASEGAWA, Ms. Honoka NIWA, Ms. Honoka WATANABE, Mr. Tomoki IKEMIZU,

Ms. Mio NAKAMURA, Ms. Hono OGIHARA, Ms. Erika KURIMOTO, and all the other former members of the Molecular Device Laboratory. Your support and camaraderie have made my laboratory experience truly invaluable.

Finally, I would like to express my deepest gratitude to my family for their unwavering support and understanding. Your love and encouragement have been my anchor throughout this journey.

This dissertation is a testament to the collective effort, support, and encouragement of all of these individuals. Thank you for being a part of this incredible journey.